Gas-dynamic trap: An overview of the concept and experimental results

Article *in* Plasma Physics and Controlled Fusion · May 2013

DOI: 10.1088/0741-3335/55/6/063001

2 authors, including:

Alexander A. Ivanov
Budker Institute of Nuclear Physics
1,165 PUBLICATIONS **37,166** CITATIONS

SEE PROFILE

Gas-dynamic trap: an overview of the concept and experimental results

2013 Plasma Phys. Control. Fusion 55 063001

(http://iopscience.iop.org/0741-3335/55/6/063001)

Plasma Phys. Control. Fusion **55** (2013) 063001 (31pp) doi:10.1088/0741-3335/55/6/063001

TOPICAL REVIEW

Gas-dynamic trap: an overview of the concept and experimental results

A A Ivanov[1,2] **and V V Prikhodko**[1,2]

[1] Budker Institute of Nuclear Physics, 630090, Novosibirsk, Russia
[2] Physics Department, Novosibirsk State University, 630090, Novosibirsk, Russia

E-mail: ivanov@inp.nsk.su

Received 7 December 2012, in final form 20 February 2013
Published 14 May 2013
Online at stacks.iop.org/PPCF/55/063001

Abstract
A gas dynamic trap (GDT) is a version of a magnetic mirror whose characteristic features are a long mirror-to-mirror distance, which exceeds the effective mean free path of ion scattering into a loss cone, a large mirror ratio ($R \sim 100$) and axial symmetry. Under these conditions, the plasma confined in a GDT is isotropic and Maxwellian. The rate at which it is lost out of the ends is governed by a set of simple gas-dynamic equations, hence the name of the device. Plasma magnetohydrodynamic stability is achieved through a plasma outflow through the end mirrors into regions, where the magnetic-field lines' curvature is favorable for this stability. A high flux volumetric neutron source based on a GDT is proposed, which benefits from the high β achievable in magnetic mirrors. Axial symmetry also makes the GDT neutron source more maintainable and reliable, and technically simpler. This review discusses the results of a conceptual design of the GDT-based neutron source for fusion materials development and fission–fusion hybrids. The main physics issues related to plasma confinement and heating in a GDT are addressed by the experiments performed with the GDT device in Novosibirsk. The review concludes by updating the experimental results obtained, a discussion about the limiting factors in the current experiments and a brief description of the design of a future experimental device for more comprehensive modeling of the GDT-based neutron source.

(Some figures may appear in colour only in the online journal)

1. Introduction

The gas-dynamic trap (GDT) concept [1–3] was proposed for a fusion reactor and a 14 MeV neutron source (NS) [3, 4] for fusion materials testing and evaluation. The original geometry of the plasma-confinement system, shown in figure 1, was proposed as an alternative to the concepts of standard magnetic mirrors.

The concept embodies a long, axially symmetric, high-β, magnetic solenoid terminated at both ends by high-field mirror magnets. The plasma confined in the solenoid is supposed to be sufficiently dense so that the mirror-to-mirror length L exceeds the effective ion mean free path of scattering into a loss cone [1, 2]:

$$L > \lambda_{ii} \cdot \ln(R)/R, \quad (1)$$

where λ_{ii} is the ion–ion mean free path and R is the mirror ratio. Then, the plasma confined in the solenoid is isotropic and Maxwellian, and the rate at which ions are lost out of the ends is on the order of the ion-acoustic speed V_{T_i}. The resulting plasma lifetime τ can then be roughly estimated as a ratio between the total number of particles in the solenoid N to their flux out of the ends $n \cdot S_m \cdot V_{T_i}$, where n is the plasma density and S_m is the plasma cross section in the mirrors. Taking into account the fact that the area of the flux tube occupied by the plasma scales as $1/R$ in the mirror throat from where the particles are lost, then [1, 2] $N \approx n \cdot S_m \cdot R \cdot L$ and $\tau \approx R \cdot L/V_{T_i}$. In the GDT, the lifetime appropriate for fusion applications can be achieved by increasing both the mirror ratio and the machine length. A fusion reactor based on GDT would, however, be quite long (e.g. $L \sim 1$ km).

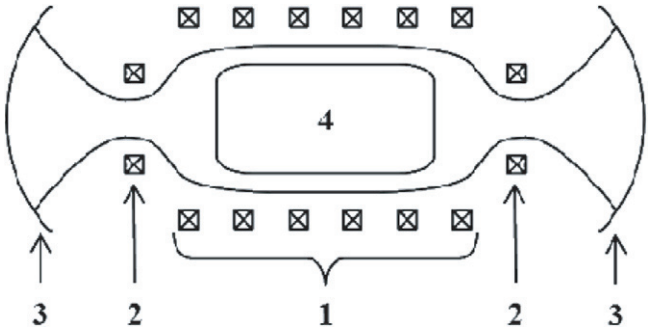

Figure 1. GDT: 1—central solenoid, 2—mirror coils, 3—plasma dumps, 4—fast ions.

It is now widely recognized that the realization of controlled fusion in reality requires a dedicated NS. This source is necessary to develop materials with long lifetimes (at least 10–15 MW yr m^{-2}, which corresponds to ∼100 displacements of every atom (dpa)) and minimal activation under neutron bombardment, and to develop components that will be needed in a fusion power plant. The GDT concept with modest electron temperature ($T_e \leqslant 1$ keV) is envisioned as an attractive D–T NS [3, 4] for material tests. Such a device of much shorter length than the reactor, operating at high beta, would provide $Q \approx 0.05$. A neutron flux of ∼2 MW m^{-2} applied to an area of ∼1 m^2 is well suited for materials testing. It has a fusion neutron spectrum and operates with low tritium consumption at efficiencies equaling or exceeding other non-fusion spectrum options [4–6].

To produce high neutron flux, energetic D and T ions with anisotropic angular distribution are produced by angled injection of ≈100 keV deuterium and tritium neutral beams at the center of the solenoid of a GDT. At a given temperature of the warm plasma and energy of the beams, slowing down of the fast deuterons and tritons via electron drag is far superior to the angular scattering of these ions. Accordingly, the fast ion angular distribution remains quite narrow, and is centered on the initial value of the pitch angle while slowing down to considerably lower energies. This results in the formation of sharp fast ion density peaks near the turning points where the ions spend a sufficiently large fraction of the bounce time. The ratio between fast ion density at the turning points and at the mid-plane varies with the injection angle θ and the angular spread of the ion distribution $\delta\theta$ as $\approx(\sin\theta)^{-3/2} \cdot \beta^{-1/2}$. It increases for shallower angles, but in practice, injection angles less than 20°–30° are not technically feasible. For the adopted energy of neutral beams, neutrons are produced mainly in collisions between fast ions. Accordingly, the neutron flux density is also strongly peaked in the same regions that house the testing zones. In contrast to the GDT-based reactor, in this case a quite moderate electron temperature of 0.5–1 keV is sufficient to generate a neutron flux as high as 2 MW m^{-2}. A GDT has the advantage of confining high-β plasmas, and the power density of fusion reactions scales as β^2. Therefore, it would be capable of producing a higher 14 MeV neutron flux density (up to 4 MW m^{-2}) than would other plasma-based sources. Note that for a magnetic mirror with quadruple min-B field, magnetohydrodynamic (MHD) stable confinement of a plasma with $\beta \geqslant 1$ has already been demonstrated [7].

In general, MHD stability is a major concern for axisymmetric mirrors, as is GDT. However, a number of methods for achieving MHD stability, while retaining the property of axial symmetry, have been proposed and explored experimentally [8–17]. Notable examples are the Phaedrus experiment at the University of Wisconsin, USA, which achieved 30% plasma beta using ponderomotive RF stabilization [18] and the AMBAL-U experiment in Novosibirsk in which 30% beta was also achieved with partial line tying to the gas-discharge plasma inside a gun placed at the end wall [19].

Originally, it was shown theoretically that MHD stability in a GDT can be achieved by a contribution to pressure-weighted curvature from the expander regions beyond the end mirrors. In these regions, the curvature of the magnetic-field lines is favorable and large enough to overcome the destabilizing effect of the axisymmetric central solenoid. This is possible because in the expander regions, beyond the end mirrors, collisional losses from the central cell sustain a non-negligible plasma pressure. On the other hand, unfavorable field-line curvature in the solenoid region can render the plasma unstable to ballooning interchange modes [20, 21]. However, a theoretical analysis indicated that $\beta \approx 1$ could be reached without encountering the ballooning instability limit. It is worthwhile to note that the GDT retains the basic advantages of a mirror system—high beta, intrinsically steady-state operation, natural ash and impurity removal, no disruptions associated with the release of magnetic energy of axial currents, as in a tokamak, low thermal and particle wall loading, etc. Additional information about the physics of mirror confinement systems can be found in the excellent survey [22]. The main advantage of the GDT is the very reliable physics of axial confinement. In contrast to other mirror systems, axial confinement physics are not sensitive to excitations of instabilities that may result in enhanced angular scattering of ions.

In the following sections, we will review the current understanding of the physics of a GDT, as derived from theory and experiment. This review begins with a discussion of the GDT-based NS concept in section 2. The experimental GDT device and the set of diagnostics are described in section 3. Several methods of achieving plasma MHD stability in a GDT, which were studied experimentally, are considered in section 4. Confinement of fast ions and bulk plasma are described in sections 5 and 6, respectively. In section 7, we summarize the main findings from the experiments on the GDT device and consider an option for a future device that should bridge the gap between the existing GDT device and a GDT-based NS.

2. GDT-based NS

Initially, as was mentioned above, the GDT [1, 2] was proposed as a possible approach to an open-ended fusion reactor. It would produce power in a long, axially symmetric, high-β, magnetic solenoid.

However, a more near-term application of the GDT concept is a 14 MeV NS for fusion materials development [3, 4] (see figure 2). In the NS, the neutron flux density

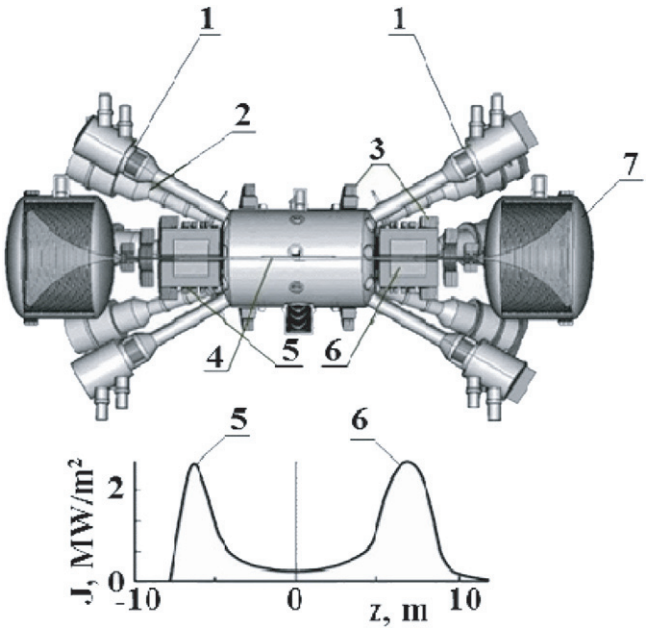

Figure 2. A GDT-based NS: 1—neutral beam injector, 2—beam dump, 3—coils, 4—plasma, 5—zone of permanent access, 6—zone of end-of-life tests, 7—expander tank. Asymmetry in the neutron flux profile is due to different gradients of the magnetic field near the turning points.

strongly peaked near the turning points of the fast anisotropic ions (figure 2, bottom). Except for these two narrow test zones, all the plasma-facing components will not suffer from intense neutron damage, and therefore will survive without replacement for a long period of time. Note that the GDT concept assumes no significant role of electrostatic plugging of the end losses, as in tandem mirrors [23, 24], and does not incorporate complex thermal barrier physics [25]. The GDT plasma contains a large fraction of collisional warm plasma to provide both MHD and micro-stability to the plasma. The initial approach [1, 2] suggested plasma stabilization against flute modes using external cells. Here, the magnetic field has favorable curvature and non-negligible plasma pressure is sustained by axial losses from the central solenoid. Other stabilization mechanisms that have emerged in the past and in recent years would be applicable for the GDT [12, 13]—including end cusp [26], non-paraxial mirror cell [16], magnetic divertor [14, 27], kinetic stabilizer [28–30], line tying [15], tail-waving feedback stabilization [31], etc. If the MHD modes are stabilized, radial transport in GDT is imperceptible, as expected in axisymmetric configurations. Then, the higher frequency wave–particle-type modes called microinstabilities, although considerably slower than the gross MHD losses, may severely limit confinement. Stimulated by the non-Maxwellian characteristic of the fast ion distribution, these modes cause particle diffusion in velocity space, with eventual loss through the mirror 'loss cone' or spontaneous redistribution of their density profile. The two microinstabilities currently predicted by theory are known to be the most dangerous for mirror-type confinement schemes. Both were observed and carefully studied in the previous mirror experiments [22]. The first is the Alfvén ion-cyclotron (AIC) mode, which is driven by anisotropy of ion pressure $P_\perp \neq P_\parallel$. It develops if plasma beta exceeds a threshold that depends on the pressure anisotropy. Another instability is related to the excitation of a drift cyclotron loss-cone (DCLC) mode. This microinstability is caused by velocity space asymmetries resulting from the loss of ions having constituent velocities within the angle of the magnetic-mirror 'loss cone.' It develops in inhomogeneous plasmas under the condition that the radial density gradient is sufficiently large. The GDT plasma is supposed to be more micro-stable against excitation of the AIC mode because the beams inject ions at an angle to the magnetic field, which reduces anisotropy of ion distribution. Additionally, their angular spread appears to be sufficiently large, especially increasing near the turning points, which is favorable for micro-stability. In addition, the beam-injected sloshing ions are imbedded in a warm plasma that also provides better micro-stability against both AIC and DCLC modes. The basic parameters for different versions of the GDT-NS are given in table 1. The electron temperature is set to be about 1% of the injection energy or less as most of the previous mirror experiments suggested. This constraint, which is based on the existing database gained for certain experimental conditions, is adopted only because of practical considerations. It is not imposed by a theory for magnetics mirrors and rather connected to quite limited available database. However, note that this limitation far exceeds what one might expect considering high possible electron heat losses to the end wall in mirrors.

In the case of GDT electron energy end loss is inhibited by the large ($\geqslant$100 fold) magnetic expansion from the mirror to the end wall [6]. As a result, the electron temperature is determined by ion confinement and far exceeds that which would result from electron thermal losses to the end walls (this topic is discussed in section 6). With further improvements in the efficiency of neutron production that suggest higher electron temperature, GDT-NS would form an attractive driver of a fusion–fission system. At a longer length and with further reduction of end losses this can be envisioned. The potential of the GDT-based 14 MeV NS as the driver of a major actinide (MA) burner was explored in [32]. The 'basic version' of the GDT-based NS, which has been proposed as an irradiation facility for fusion material research, turns out to deliver about one order of magnitude less neutrons than would be necessary for a burner of commercial scale used to burn toxic nuclear waste, produce fission fuel, or electricity. The hybrid concept application requires a plasma Q of 2–5 [33, 34].

The power balance of the MA burner and its efficiency in the destruction of trans-uranium isotopes by fission for the basic version of GDT-NS appeared to be considerably less competitive than the spallation and tokamak-based burners. An increase in the electron temperature of the GDT plasma up to 1.5–3 keV would result in an efficiency of the GDT-based MA burner that is comparable to that offered by a tokamak-based and exceeds that of a spallation source. The realization of this possibility demands further plasma physics research. In addition to this, the GDT-NS offers the possibility of longitudinally stretching its neutron production volumes. In this way, the total strength and the energetic efficiency of

Table 1. Parameters of GDT-based NS [35].

Parameter	Beam–plasma version	Beam–beam version	Fully SC version
Tritium beam energy (keV)	240	94	65
Deuterium beam energy (keV)	—	80	65
Tritium beam power (MW)	20	6.5	20
Deuterium beam power (MW)	—	8.5	20
Electron temperature (keV)	0.6	1.1	0.65
Plasma density at the mid-plane (m^{-3})	2×10^{20}	2×10^{20}	2×10^{20}
Plasma radius at the mid-plane (m)	0.06	0.08	0.06
Mirror ratio	20	15	10
Magnetic field at the mid-plane (T)	1.25	1.8	1.3
Injection angle (°)	20	40	30
Max. neutron flux ($MW\,m^{-2}$)	3.9	1.8	1.8
Power consumption (MW)	50	60	47

the source can be substantially increased. Encouraging results were obtained from the study [32] of a longitudinally extended burner. Both measures together would greatly improve the characteristics of the GDT-based sub-critical MA burner and make it fully compatible with other proposed schemes.

Accordingly, the physical issues to be studied for the GDT-NS include demonstration of adequately high electron temperature, steady-state operation, ballooning instability threshold, plasma equilibrium at high β, effect of ambipolar fields on confinement, effect of plasma rotation on confinement and radial transport, etc. The efficiency of different MHD stabilizers at relevant plasma temperatures and densities, as well as the applicability of auxiliary plasma heating (ion-cyclotron resonance heating (ICRH), electron-cyclotron resonance heating (ECRH), axial injection of electron beams) methods should be studied in addition. Moving from physics to engineering issues, first note that engineering design constraints for GDT-NS are eased due to its axial symmetry and the lack of considerable axial plasma currents, which otherwise could result in catastrophic plasma disruptions, as it happens in tokamaks. Then, a high-pressure plasma can be sustained with steady exhaust power beyond the magnet system, which does not undergo large variations. Design of axially symmetric magnetic coils utilizes already demonstrated technologies except for the versions with very high magnetic field in the end mirrors. The remaining major issues are development of continuous neutral beams with 65 keV or higher energy and 40 MW power with small divergence and focusing (prototypes already exist [36]), handling plasma exhaust ($\sim 10^{22}$ particles s^{-1}), neutron shielding of sensitive elements and a high-frequency ($\sim$1 kHz) pellet injector for sustainment of warm plasma that has a lifetime on the order of milliseconds.

The problems of the neutron shield for the GDT-NS equipment that are critically sensitive to irradiation were considered in [37]. Starting from a crude, non-optimized over-shielding placed everywhere between the plasma and the coils leaving only space for injected neutral beams (to check the feasibility of survival protection), simulations were run to establish the damage on the sensitive components. It was shown that due to neutron streaming along the neutral beam lines, the extreme local dose of neutrons on the exposed ion-head insulating alumina and that on the bending magnet insulator allows a survival of the parts beyond the natural service life of the ion source once a local adequate shield is inserted. Thus, the protection is such as to make replacement interventions determined by the natural consumption of the ion source, not by radiation damage. Among the magnets, the most critical ones are those in direct contact with the injector ducts that hinder good shielding. The central one, and the most critical one, was shown to be at the limit of tolerance of the displacement per atom (dpa), while safe for other parameters. Its shield has been redesigned and the coil is now expected to outlive the GDT-NS 10-year operation period. Although the above results were derived from the non-optimized crude shield, simulations already show that the GDT-NS operation at the current level of concept of design and shielding is viable. Several design modifications have been suggested to improve GDT-NS properties, and some of these suggestions have been evaluated.

In order to cope with the steep gradients in the testing zones of the GDT-NS, the use of miniaturized specimens was suggested [38], already a common practice in the fusion materials community. The 'small specimen test technology' (SSTT) is an ongoing, facility-independent activity aimed at developing suitable miniaturized specimens and testing techniques for qualifying irradiated structural materials [39, 40]. The proposed GDT-NS tubular test assembly (TTA) must be capable of accommodating a variety of materials ranging from metals to non-metals, and must be capable of adjusting and controlling specimen temperatures. The design principles of the adopted TTA design follow safety, reliability and maintainability criteria previously developed for the IFMIF project [41] and include simplicity, fail-safe and fault-tolerant design, structural integrity and compatibility, as well as testability.

Helium gas is adopted as a coolant as it is inherently safe, has good compatibility with structural materials, some of which will be at elevated temperatures, does not become activated and significantly simplifies any remote handling manipulations. The helium-cooled TTA is a vessel-type hollow cylinder with 10 irradiation rigs of 2 m length. Each of the eight rigs dedicated to structural materials contains eight specimen capsules at the desired irradiation temperature, while two or three specimen capsules might be sufficient for the two rigs reserved for ceramic breeder materials. Figure 3 shows a

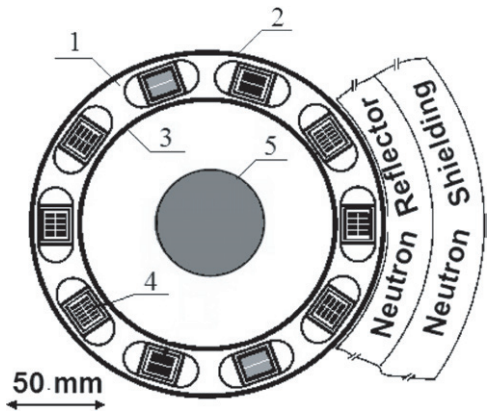

Figure 3. Schematic cross-sectional view of the TTA: 1—He gas coolant, 2—cover tube, 3—vacuum chamber, 4—miniaturized specimens, 5—plasma.

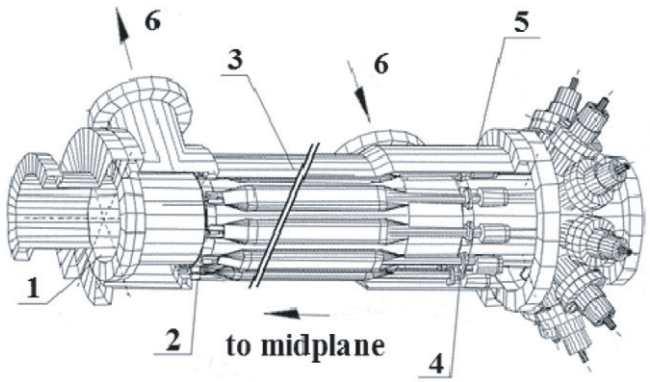

Figure 4. Elevation view of the TTA: 1—vacuum chamber, 2—sliding support, 3—rig, 4—rig attachment, 5—cover tube, 6—He gas coolant.

cross section of the TTA with the plasma tube surrounded by the helium gas cooled rigs, and the cover tube. The interior of the rigs closely follows a coolant concept developed recently for IFMIF [40–42]. Individual irradiation temperatures can be achieved using gas gaps between the specimens and capsules as well as between the capsules and rig walls, a common procedure in materials test reactors. This keeps the structural materials (capsules, rigs and TTA structure) at moderate temperatures well below the specimen temperature during irradiation.

The use of gas gaps to rise the specimen temperatures means that the entire irradiation window (300–1000 °C) is independently available not only for each rig but even for each individual specimen capsule. Apart from the passive temperature control with individual gas gaps and the tuning of the He-gas coolant, during normal operation it might be desirable to adjust the individual capsule temperature. Therefore, it is planned to integrate an ohmic heating system into each of the 20 cm long specimen capsules. This system would also be used for temperature control during plasma-instability and plasma-off periods. Although one type of specimen is currently foreseen for each capsule, the capsules could also be assembled with different specimen geometries.

The two rigs dedicated to tritium release experiments can be assembled with a few capsules that would be filled with different types of ceramic specimens. Tritium released by the specimens in the capsules will be swept away by helium gas, which will flow continuously through the capsules, and will be then carried through very thin pipes to the analyzing equipment located in the vicinity of the mirror machine.

The design of the completely assembled TTA capable of accommodating as many as 8000 miniaturized specimens in a volume of 20 l is illustrated in figure 4. Test samples are located outside of the vacuum wall, so that samples can be changed without an air cycle, and mechanical and electrical stresses can be applied and measured more conveniently.

The MCNP model of the GDT-NS was used to simulate the neutron conditions in the helium-cooled TTA in the material test irradiation zone. The TTA is backed in the radial direction by a 12 cm thick steel reflector and a 28 cm thick shield (90 vol% tungsten, 10 vol% water). Calculations were performed with the MCNP Monte Carlo code, taking into account about 7 million source neutron histories and resulting in statistical errors well below 1% for each of the calculated responses.

Radial–axial profiles were calculated for the neutron fluxes, the dpa and the gas production rates in the TTA region. The maximum dpa rate in the TTA is at about 15 dpa/full-power year (FPY) and the largest fraction of the TTA volume will be at the dpa level of 10–15 dpa/FPY that is sufficient for materials testing. The variation in dpa/FPY, resulting from the neutron flux gradient, is about 15% cm^{-1} in radius, 0.5% cm^{-1} along the axis, and zero in azimuth, better than the 20% cm^{-1} requirement for materials irradiation testing.

Studies in Russia and the US [43–45] have produced several conceptual designs of 14 MeV fusion NSs based on the GDT concept. The physical sizes are similar to GDT but typically use four times higher magnetic fields and neutral beam injection (NBI) energies. The required power, typically 40 MW, is dependent on the electron temperature. Simulations [46] indicate an approximate 14 MeV neutron power flux dependence of

$$P/A = 2.5T_e\,(\mathrm{keV})\,\mathrm{MW\,m^{-2}}. \qquad (2)$$

Equation (1) is satisfactory for neutral beam energies in the range 65–105 keV. Note that for the 0.2 keV electron temperature achieved in the GDT experiment, equation (2) predicts a neutron flux of 0.5 MW m^{-2}, comparable to that projected for ITER.

Compared with accelerator-type NSs, GDT-NS would provide a 100-fold larger test volume and would produce a 14 MeV fusion energy spectrum. Tokamak sources would also provide a 100-fold larger test volume but need to breed tritium due to the high rate of tritium burn-up.

There are issues with the GDT-NS concept. The main physics issues are scaling of electron energy transport, axisymmetric MHD and micro-stability. While theoretical analysis is positive, experimental confirmation needs to be demonstrated. The key technology issues are truly steady-state neutral beams, tritium reprocessing and retention, and vacuum pumping. While challenging, these technology issues are common to all magnetic-field concepts.

One of the advantages of the GDT-NS is a relatively low tritium consumption (about 150 g per year), in addition to a relatively low tritium inventory in the GDT-NS device (less than 500 g). To simplify technically the system of deuterium–tritium gas processing, the two-component atomic beam injectors used for the D–T mixture are being further developed. In this case, there is no need to carefully separate deuterium and tritium, and one can use cryogenic panels with different temperatures as a sufficient separation scheme. The experiments were conducted in Novosibirsk with a 40 keV, 1 MW, 1 s neutral beam to support this idea [47]. The ion source was operated with a D–H mixture, which was supplied directly to the plasma box through a pulse valve. The relative concentration of deuterium in the mixture was varied from 0% to 100%. The results of perveance scans indicated that at an optimized level the extracted ion current corresponded to an effective mass of plasma ions in agreement with the Child–Langmiur law, as expected.

Other applications of the GDT approach, requiring an intermediate performance between a NS for materials testing $Q = P_{\text{fusion}}/P_{\text{input}} \sim 0.05$ and pure fusion $Q > 10$, are the fusion–fission hybrids. For this application $Q \sim 1$ would be sufficient, which can be realized [34] at relatively low electron temperatures in the range of 3 keV, with a plasma diameter of 1 m and mirror-to-mirror length of 40 m. Studying the Q required for economical burning of fission reactor wastes by fissioning transuranics with multiplication of fusion's neutron energy by a factor of ∼10 or more indicated that a Q less than 2 would be sufficient. For a minor actinide burner with multiplication over 50, an even smaller $Q \sim 0.2$ would be sufficient [34, 48].

It is worth noting that capabilities of the GDT-based NS can be additionally extended if the neutron flux can be modulated with a desired frequency. The modulation may be an enabling tool for the assessment of the role of non-steady-state effects in fusion devices as well as for high-precision, low-signal basic science experiments favoring the use of the synchronous detection technique. In [49] a conclusion is drawn that a modulation frequency of up to 1 kHz and a modulation amplitude of a few percent are achievable. Limitations on the amplitude of modulations at higher frequencies are also discussed in [49]. A specific approach to modulation of the neutron flux by producing periodic short-lived density peaks near a turning point if the injection energy is properly modulated in time is considered in [50]. It is shown that the bunching of deuterium and tritium ions can produce periodic short bursts of neutron radiation with intensity 1.5 times higher than the average level.

Summarizing this section, it is worthwhile stressing again the advantages of the proposed NS for materials development. The neutron flux of $\sim 2\,\text{MW m}^{-2}$ to an area of $\sim 1\,\text{m}^2$ is well suited for material testing. The device produces a fusion neutron spectrum and operates with low tritium consumption at efficiencies equaling or exceeding other non-fusion spectrum options. The characteristics of a GDT-based NS, as a magnetic-mirror plasma-confinement device, make it particularly appropriate [43, 51–54]:

- Inherently steady-state operation, but can be modulated at a few kHz if desired. An extensive international database has been developed for pulsed magnetic mirrors. The needed steady-state database could be generated during hydrogen operation of a NS, before completing the shielding and nuclear technology portions of the facility, or in a separate facility.
- High beta confinement, $\beta \sim 1$ (i.e. the plasma pressure is equal to the magnetic-field pressure). This enables a high flux of neutrons to be created in small volumes of a few liters.
- It can also provide a $1–2\,\text{MW m}^{-2}$ neutron flux over the larger volumes (∼100 l) needed to develop tritium-breeding blankets.
- Electron temperatures can now reach classical values, using techniques that are understood theoretically, and demonstrated experimentally, to suppress secondary emission [55, 56]. This reduces the heating power for a given neutron production.
- Low tritium consumption ($\leqslant 0.2\,\text{kg yr}^{-1}$ so that tritium can be purchased and is not required to be bred *in situ*) and a low tritium inventory for safety. Tritium breeding can be developed in this facility.
- High neutron flux ($>2\,\text{MW m}^{-2}$) in test zones allows accelerated testing of materials in volumes exceeding 1 l.
- Significantly lower neutron flux at the facility walls ($\leqslant 0.1\,\text{MW m}^{-2}$) and low heat ($\leqslant 0.6\,\text{MW m}^{-2}$), so the facility is not being 'tested'.
- The primary neutron spectrum is that of deuterium–tritium, with no high-energy tail, as in accelerator-based NSs (spallation or D-LI IFMIF type).
- Simple, therefore inexpensive, magnets.
- Can use well-tested positive-ion neutral beams, extended from current operation to steady state.
- The flaring of the magnetic field in the end tanks allows one to reduce the heat flux on the plasma dumps to a manageable level of $1\,\text{MW m}^{-2}$ or less.
- Only fusion-relevant technologies used: neutral beam or possibly RF heating, superconducting magnets, tritium handling, steady-state power plant operation (with $Q < 1$).
- Cost is ∼10% of ITER.
- Hydrogen operation allows commissioning without radiation issues.

3. Experimental setup and diagnostics

The experiments in support of development of a GDT-based NS are carried out in Novosibirsk, in the GDT device. The GDT magnet and neutral beam systems are shown in figure 5. The vacuum chamber consists of a cylindrical central cell 7 m long and 1 m in diameter and two expander tanks attached to the central cell at both ends. A set of coils mounted on the vacuum chambers produces an axisymmetric magnetic field with a variable mirror ratio ranging from 12.5 to 30 when the central magnetic field is set to 0.3 T. In some experiments,

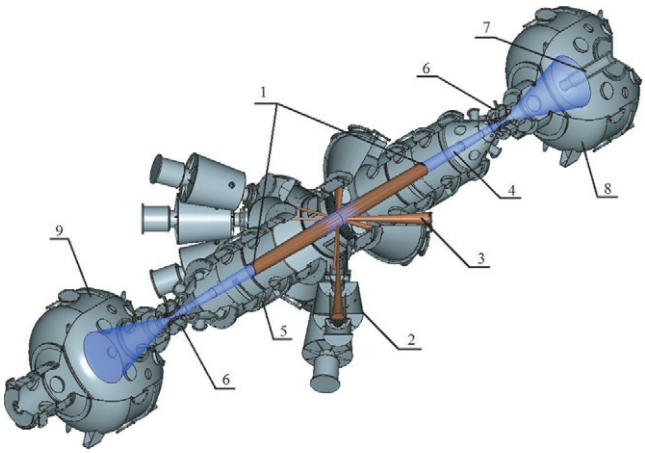

Figure 5. Cutaway view of the GDT device: 1—fast ions turning points, 2—neutral beam injector, 3—beam dump, 4—warm plasma, 5—coils of the central solenoid, 6—mirror coil, 7—plasma gun, 8, 9—expander tanks.

Table 2. Parameters of the GDT device.

Parameter	Value
Mirror-to-mirror distance	7 m
Magnetic field at the mid-plane	Up to 0.35 T
in mirrors	2.5–15 T
Bulk plasma density at the mid-plane	(1–6) $\times 10^{19}$ m^{-3}
Bulk plasma radius at the mid-plane	6–7 cm
Electron temperature	Up to 250 eV
Energies of deuterium/hydrogen neutral beams	20–25 keV
Neutral beams' pulse duration	5 ms
Total injection power	Up to 5.4 MW
Injection angle	45°
Fast ion density in turning point regions	$\approx 5 \times 10^{19}$ m^{-3}
Mean energy of fast ions	$\approx$10 keV
Maximal local plasma β	Up to 0.6

this configuration was modified by adding compact mirror cells at both ends of the GDT central solenoid. The basic parameters of this device and the plasma parameters typical for the operational regime are listed in table 2. Typical time evolution of some parameters is presented in figure 6.

MHD stability of the finite-β plasma in the central solenoid, within certain limits set by the experimental scenario, was achieved by using the axially symmetric end cells where magnetic-field lines have favorable curvature. Remote anchor cells of two different types were experimentally tested. The first is an expander end cell in which the plasma from the mirror throat freely expands along the gradually decreasing magnetic field up to the end walls. The field inside the expander end cells is formed by a combination of the stray field of the solenoid and the field of a large radius expander coil mounted on the end tanks (see figure 5). The current in this coil was normally opposite to that of the solenoid coils. In this case, the field lines in the expander curve away from the axis, which is favorable for stability. An additional coil set in one of the end tanks formed a cusp end cell where there is a magnetic field null on the axis. By energizing the proper coils of the end tank, we were able to perform experimental runs that switched between expander and cusp end cell configurations without

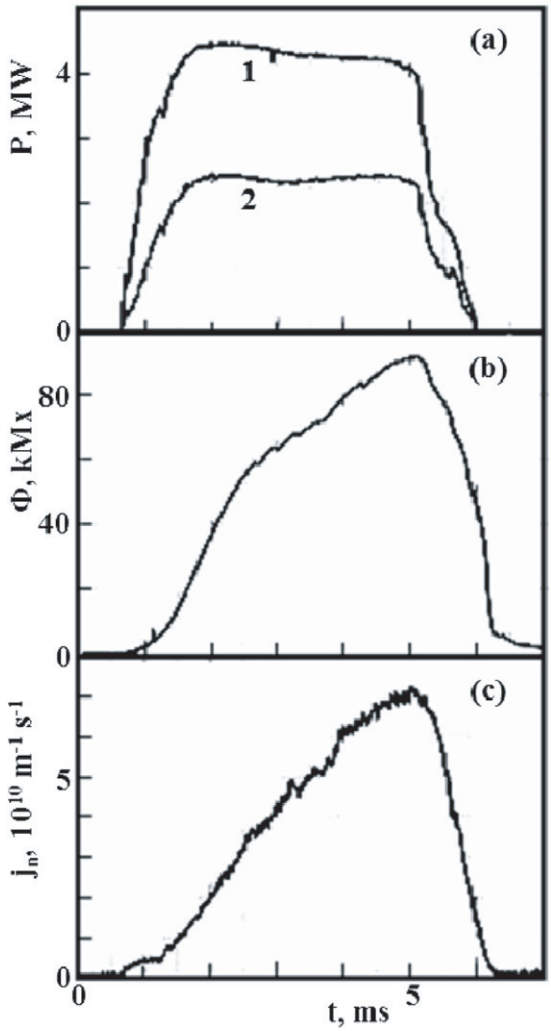

Figure 6. Time evolution of representative shot parameters: (*a*) injected (1) and trapped (2) power, (*b*) diamagnetic flux at the turning point, (*c*) neutron yield density.

opening the device to air. A sufficiently high plasma density was maintained in the end cells by collisional losses of the warm plasma from the central solenoid. In the expander end cells, the plasma flowed during one transit and dumped on the end plates, whereas in the cusp end cell, plasma stayed for several transits and accumulated during a shot. The ring cusp was 53.5 cm in radius, and the magnetic field in the cusp was maximally set to 1.76 T. The outboard point cusp magnetic field was 2 T.

In separate experiments, we employed a set of biased radial limiters and radially segmented end walls to control the electric field in the plasma. While varying the electric field, a maximum in plasma energy and diamagnetism was observed. Later on, it was understood that radial plasma losses in the regimes with biasing of the end plates and radial limiters could be reasonably small even if the MHD stabilizing end cells were not engaged. This happens when the radial limiter and the outer ring of the end plates were biased at $\sim$150 V, while the inner segments of the end plates were electrically floated. In this regime of operation, which is considered in further detail in this section, the radial extent of the warm target plasma remained almost unchanged during NBI. This indicates that

Table 3. Characteristics of the GDT neutral beams.

	Parameter spread	Total
Extractedion current (A)	35–45	330
Beam energy (keV)	23–24	
Ion beam power (MW)	0.81–1.1	7.7
Angular divergence (mrad)	18–21	
Beam neutralization efficiency	0.85–0.86	
Beam line acceptance	0.73–0.95	
NB power incident on the plasma (MW)	0.51–0.83	about 5.4

no enhanced radial transport precludes the production of high-β, multi-component plasmas in a GDT configuration.

In the experiments, the GDT plasma was heated and fast ions were produced by injection of 6–8 deuterium/hydrogen neutral beams [57]. Neutral beam currents in excess of maximally 320 equivalent atomic amperes were injected with an accelerating voltage of 23–24 kV. The maximum beam duration of each injector is set to 4–5 ms. Under the typical conditions of experimentation, about 2.6 MW were trapped by the solenoid plasmas. The characteristics of the GDT neutral beams are presented in table 3.

The initial plasma is produced by a ≈3 ms pulse from a washer stack hydrogen-fed plasma gun. The gun is located in one of the end tanks beyond the mirror throat. Under standard conditions, within ≈3 ms, the plasma density reached $(5–7) \times 10^{19}$ m^{-3}, after that the gun current was terminated and the plasma began to decay. The electron temperature of the gun-produced plasma (3–10 eV) was nearly constant across the radius. The radial density profile was well fitted by a Gaussian distribution with a characteristic scale length of 6–7 cm, which slightly changed with the magnetic-field strength in the gun. During beam injection, significant broadening of the density profile was observed.

In order to decrease the charge-exchange losses of fast ions it is essential to reduce the neutral gas recycling at the chamber wall. For that purpose, an array of electric-arc Ti-evaporators was installed inside the central cell of the device. The arrangement of the evaporators and the application procedure were optimized to allow fast and homogeneous coating of the wall surface just before a plasma shot. To improve the adhesion of the film to the wall, the inner surface of the chamber was covered by stainless-steel panels, which have undergone several special treatments including sand blasting of the plasma-facing surface and baking out at a high (∼800 °C) temperature. Application of the installed evaporation system increased the mean charge-exchange lifetime of the fast ions from 1 ms up to 10 ms and made it much longer than the fast ion particle confinement time and their slowing down time. This was mainly achieved by a drastic reduction of the fast neutral recycling at the Ti-coated first wall. Thus, the base pressure in the central cell during the shots was sustained at a level of $(0.5–1.1) \times 10^{-5}$ Pa. A detailed description of the vacuum system, Ti-evaporation system, wall preconditioning procedure and the experiments concerning the dynamics of the neutral gas in the GDT during the NB injection is presented in [58].

The plasma parameters at the solenoid were measured with a number of diagnostics [59]. The density profile is derived from the measured attenuation of neutral beams and from Thomson scattering data near the mid-plane. The Thomson scattering system also measured the electron temperature in the plasma core. These data were combined with those from the probes installed in a radial limiter shadow to provide the electron temperature profile. Temporal variation of the ion temperature of the target plasma was measured by Rutherford scattering of a diagnostic neutral beam (DNB) [60–62]. At the end of the beam injection pulse, the ion temperature was close to that of the electrons [63].

In order to measure the radial profile of plasma beta in the turning point region we applied a motional Stark effect (MSE) diagnostic [64]. It utilizes the effect of the Lorentz electric field $E = [v \times B]$ appearing in the frame of reference of a fast atom moving in a transverse magnetic field. For a hydrogen atom, the resulting Stark splitting is linear in the magnetic field. Therefore, it provides a robust method of local magnetic-field measurements. By measurements of the absolute value of the magnetic field in plasma shots and in vacuum shots, one can calculate the plasma diamagnetism as $\Delta B/B = (B_{\rm vac} - B_{\rm plasma})/B_{\rm vac}$. Ideal (single-fluid) MHD in paraxial approximation (negligible field line curvature) gives perpendicular pressure balance equation of the form

$$B^2_{\rm vac}/8\pi = B^2_{\rm plasma}/8\pi + P_\perp.$$

Using this equation one can further estimate the plasma beta as

$$\beta = P_\perp/(B^2_{\rm vac}/8\pi) = 2\Delta B/B - (\Delta B/B)^2.$$

The MSE diagnostic on the GDT comprised of a DNB injector [65] and a registration system. The spatial resolution was determined by the diagnostic beam size and by the viewing angle of the observation system. It was 4.5 and 1.5 cm along the viewing chord and in the perpendicular plane, respectively. The temporal resolution was 200 μs, as it was set up by the duration of the diagnostic beam.

Neutral beam attenuation detectors are used to measure the trapped power of the heating beams. The target plasma-energy content and that of the fast ions were inferred from the diamagnetic loop data. One of those loops was located at the mid-plane and another beyond the turning points of the fast ions. The charge exchange and radiation losses from the plasma were measured by a set of pyro-bolometers having a time resolution of 10 μs. Near the mid-plane, the fast ions are partially neutralized by charge exchange with the neutral gas components and leave the plasma within rather a small interval of pitch angles near the injection angle of 45°. A bolometer located at the mid-plane is used in conjunction with a movable collimating tube aimed to separate the charge exchange of fast ions and the radiative losses from the plasma column. A detailed description of these diagnostics is given in [58, 66].

To monitor the time evolution of the radial density profile a diagnostic based on the charge exchange of a 25 keV D^0 beam was developed [67]. Its spatial resolution was 1.5–2.0 cm and its time resolution was 50 μs. Fast inverse magnetron ionization gauges were used for the measurements of the

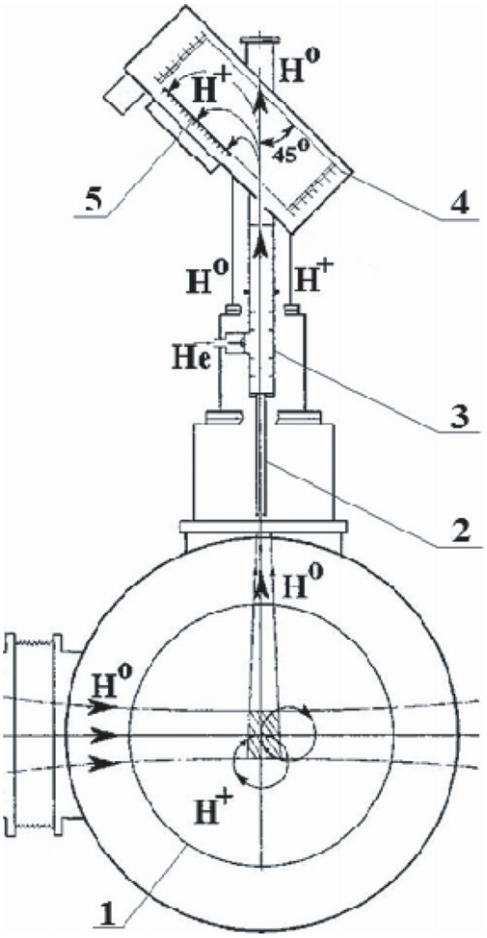

Figure 7. Layout of the diagnostic to measure the local energy distribution function of fast ions: 1—plasma, 2—collimator, 3—stripping cell, 4—electrostatic 45° analyzer; 5—12-channel detector.

time evolution and spatial distribution of neutral gas density inside the central cell [58]. The parameters of the fast ions were measured using an artificial target method, neutral particle analyzers, and an array of diamagnetic loops and magnetic probes installed at different axial locations inside the solenoid [68].

The local energy distribution function of fast ions was measured by means of an artificial target method [69, 70]. For that a diagnostic hydrogen neutral beam injector was installed in the central plane of the device at a distance of 1.2 m from the axis (figure 7). The energy of the neutral beam was 13–15 keV in a different series of experiments, the beam current was up to 25 atom amperes and the pulse duration was 120 μs. In order to increase the neutral beam density in the plasma an ion optic system which provides beam focusing was used [70]. Because of this the beam radius at the focal point was about 2 cm, and the current density up to 0.5 atom A/cm^2. The neutral beam was employed as a charge-exchange target for the fast ions. The charge-exchange neutrals escaping from the plasma near the mid-plane were analyzed by a 45° electrostatic charge-exchange particle analyzer (CXA). The energy analyzer consists of a helium stripping cell, a 90° deflection parallel plate energy analyzer and a 12-channel detector based on a microchannel plate. The CXA scans

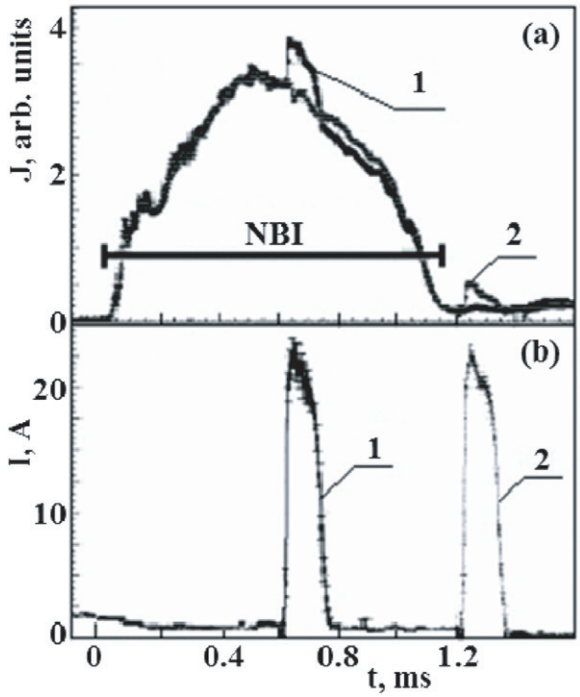

Figure 8. Time evolution of the total neutral particle flux (a) and the neutral beam current of the diagnostic injector (b) in two experiments.

the energy range from 2.8 to 20 keV. Shifting the analyzer to different positions along the machine axis from shot to shot and/or varying the inclination angle allow measurement of the angular distribution of fast ions. The limits within which the inclination angle can be varied at the mid-plane were $45 \pm 5°$. The angular resolution of the analyzer varied at different axial positions in the range 0.35°–0.8° and its energy resolution within the range 0.4–1.3 keV. Figure 7 shows the layout of the diagnostics.

The local measurements were rather complicated because of the presence of the heating neutral beams, which are injected at the same place and provide a high charge-exchange background. A typical time evolution of the total neutral particle flux measured by the CXA along with the time evolution of the DNB current is shown in figure 8 for measurements before and after switching off the main neutral beams. The background observed is associated with the charge exchange of fast ions on the neutral components: warm neutral atoms generated by charge exchange of neutral beams, peripheral cold neutrals and heating neutral beams. Since the neutral particle fluxes resulting from fast ion charge exchange on the diagnostic beam were relatively small, the fluctuations of the background neutral fluxes played an important role. Therefore, the required accuracy of the measurements of the distribution function (±10%) was reached by averaging the data over several experimental shots. The relationship between the current in a registration channel of the CXA, $J(E)$, and the energy distribution function of the fast ions, $f_{\mathrm{F}}(E, r, \theta)$, can be written as

$$J(E) \sim K_{\mathrm{He}} K_{\mathrm{att}} f_{\mathrm{F}}(E, r, \theta) n_{\mathrm{b}} \sigma_{\mathrm{ex}} v \Delta\theta \Delta E V,$$

where n_b is the diagnostic beam particle density, $\sigma_{ex}v$ is the charge-exchange rate of fast ions with energy E on the target gas, V is the plasma volume seen by the analyzer (typically $8 \times 6 \times 2.5\,\text{cm}^3$), $\Delta\theta$ and ΔE are its angular and energy resolutions, K_{att} is the factor accounting for fast neutral attenuation in the plasma and K_{He} is the stripping efficiency in the CXA helium cell. This relationship was used to calculate the fast ion distributions from CXA data.

The diagnostic hydrogen neutral beam injector and the electrostatic analyzer were also used to measure the effective ion drag time in the target plasma (see section 5). Radial profiles of charge-exchange fluxes were measured by a modified electrostatic analyzer [71] (see section 5).

The plasma parameters in the end tank opposite to that where the plasma gun is placed were measured using the following diagnostics:

- a movable emissive (flashing) probe which measures the plasma potential,
- a movable gridded probe which measures the ion flux density,
- a movable bolometer for measurements of the energy flux density,
- an electrostatic end-loss analyzer (ELA) for measurements of the ion energy distribution function,
- a movable Langmiur probe for measurements of the mean electron energy and the plasma potential.

The probes and the bolometer were installed at a movable support at an axial stroke of 120 cm that allows their insertion directly into the mirror in one of the extreme positions. The ELA could be installed at the end wall on the axis of the expander instead of the support.

Additionally to the probes, the method of a local gas target with the use of ELA was employed to measure the plasma potential along the expander axis. The target was produced by a pulsed gas supply through a glass capillary, which was moved along the device axis from shot to shot. The cold ions produced due to charge exchange and ionization of the particles of a gas cloud were accelerated by the ambipolar electric field. The energy of accelerated ions, which was measured at the end wall by ELA, corresponded to the potential at the point at which charge exchange occurred.

4. MHD stability and radial plasma losses in the GDT

In this section, the results of the study of MHD plasma stability in a GDT will be reviewed. In the initial experiments, the stability of a gun-produced plasma in the configuration with the expander end cells was studied. Regardless of the magnetic-field configuration, whether it was favorable for stability or not, there were no indications of instability growth and enhanced plasma losses within certain limits during the plasma build-up. We attribute that to the line-tying mechanism [72]. Namely, it was suggested that azimuthally directed charge separations due to flute instability growth are inhibited by currents flowing along the field lines from the gas-discharge plasma inside the gun, which is supposed to be highly conductive across the magnetic field.

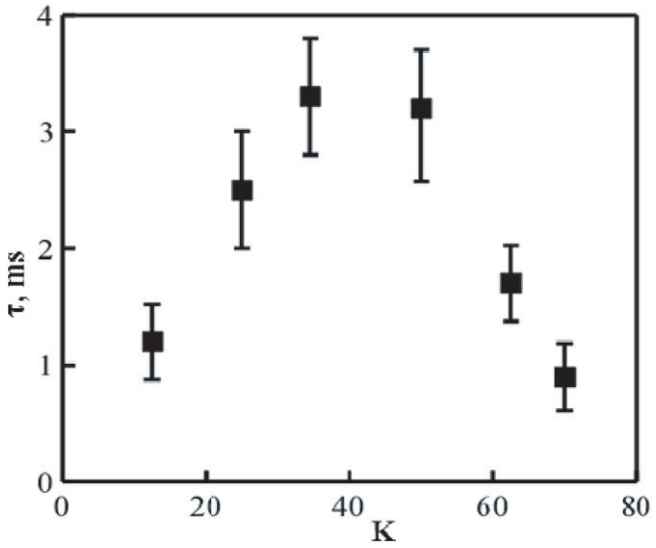

Figure 9. Plasma decay time versus mirror ratio.

While the gun was turned on, the plasma density increased approximately linearly in time. After the discharge current was terminated, the behavior of the decaying plasma became sensitive to the curvature of the field lines inside the expanders. The decay time and amplitudes of density fluctuations measured by the probes indicate whether the plasma is stable or not. While the 'expander' coils were not energized and the field lines in the expander were almost straight lines with negligible curvature, it resulted in growth of flute-like perturbations and enhanced plasma losses. It should be emphasized that strong alterations of the curvature inside the expander caused negligible changes of the field in the central cell. In fact, switching the current on and off in the expander coil produced relative changes of the order of 10^{-3} of the central cell field. On the other hand, parameters of decay in the case of a favorable averaged curvature agree well with theoretical estimates of axial plasma losses through the mirrors [51, 73]. One can conclude from these data that the axial plasma flow into the external region with a sufficiently large favorable curvature stabilizes the internal cell. Reducing the external curvature resulted in reduction of particle confinement time of the internal cell. Thus, the mechanism of stabilization by an expander end cell was vividly displayed [73].

Stability limits relative to other essential parameters of the plasma and magnetic field were also studied. The results are presented in figures 9 and 10. Longitudinal plasma losses from the central cell provided the plasma to the expander for the suppression of MHD instability. As increasing the mirror ratio decreased the plasma loss, the plasma pressure inside the expander was reduced, allowing the instability to develop in the whole system. Figure 9 demonstrates the transition from stable to unstable regimes of confinement due to reducing the plasma pressure in the expander when the mirror ratio was varied from 12.5 to 70. The expected linear relationship of lifetime versus mirror ratio was valid for mirror ratios smaller than the

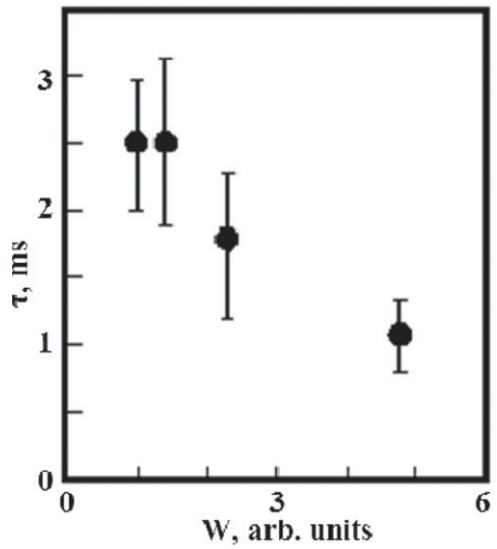

Figure 10. Plasma decay time versus averaged curvature in the central cell.

stability boundary at $R_m \sim 40$. Plasma lifetimes at higher mirror ratios, in contrast to those expected by particle balance considerations, decreased even as plasma loss rates through the mirrors were reduced. Beyond the stability boundary, fast growth of large-scale perturbations of the plasma column was registered by all diagnostics used. Measured growth rates and longitudinal wave numbers of unstable modes were in reasonable agreement with theoretical estimates. In addition, we observed a similar transition when the instability drive in the central cell was increased at fixed expander parameters (see figure 10). To show this, we varied the curvature in the central cell by changing the current in the coils located near the mid-plane. Below a particular additional curvature in the central cell the plasma decay was quiescent. Above this level, flute-like low-frequency fluctuations developed in the plasma. This behavior can be interpreted as evidence of a stability boundary. The data presented in figures 9 and 10 are in reasonable qualitative agreement with the theory of Rosenbluth and Longmire [74] that uses pressure-weighted curvature criterion, somewhat modified to take into account the plasma directed velocity in the expanders:

$$\int \frac{(P_\perp + P_\parallel)\kappa}{B^2 r}\,\mathrm{d}s \geqslant 0,$$

for stability. Here s is a coordinate along the field line, $P_\perp$ and $P_\parallel$ are the components of the pressure tensor, and κ is the normal curvature. For paraxial (long-thin) axisymmetric mirror systems $s \approx z$ and this stability criterion can be rewritten in a particularly simple form [75]:

$$\int (P_\perp + P_\parallel)a^3 \frac{\mathrm{d}^2 a}{\mathrm{d}z^2}\,\mathrm{d}z \geqslant 0, \qquad (3)$$

where $a(z)$ is a radius of the plasma boundary that lies on one of the flux surfaces. This criterion is written for the case of a radially uniform plasma with a sharp boundary, but it contains all the substantial features of a general criterion. Note that larger plasma radii (i.e. smaller magnetic fields, as in the expander region) zones make a stronger contribution to the integral (3). Thus, the plasma pressure in the expander can stabilize the system. Of course, this plasma exhaust is of relatively low pressure, but due to the a^3 weighting of the stability integral, the contribution to stability is significant. To assess the plasma stability, these integrals were calculated for the field line corresponding to the maximum pressure gradient. In fact, if here the integral is positive, the plasma is to be stable against excitation of the small-scale flute modes, which are localized in this region. Note that a higher positive value of the integral, or a favorable pressure-weighed curvature, is better. In a state with a higher averaged curvature, the plasma equilibrium acquires more 'rigidity' against external disturbances, e.g. azimuthal asymmetry in heating and fueling, multipole disturbances of the magnetic field, which, in particular, was confirmed by special experiments [76]. The calculated contribution to the pressure-weighted curvature of the expanders, and the contribution estimated from the experimentally observed stability limit were found to have a quantitative difference of ~5. The reason for this is still unclear. The observed quantitative difference with predictions of the ideal MHD theory might be connected with some additional effects in the expander. Those induced by the finite resistivity of the end plates were considered in [77]. The finite plasma resistivity may also account for the discrepancy, especially at the lowest plasma temperatures [78]. Calculations of the expander's contribution to stability were performed through the use of adiabatic and isothermal models of plasma flow in the expander. Experiments [79, 80] indicated that the regime of plasma flow significantly differed from both and approached the flow predicted by the adiabatic model only for regimes with auxiliary heating. Additional effects may also arise from the finite ion Larmor radii in the expander when they become comparable to the curvature radius or the plasma radius in the expander. Finite β and non-paraxiality may also contribute to the observed quantitative difference. This stability criterion was also quantitatively tested in tandem mirror experiments [81, 82]. In [81], a considerable (factor of 6) quantitative difference was also noted. A more detailed description of the experiments to study stability of the gun-produced plasma is given in [51].

When the plasma crossed the stability boundary, large-amplitude, low-frequency (6–25 kHz) fluctuations were observed to have features similar to MHD flute modes. We investigated the axial variations of these fluctuations. At electron temperatures of 5 eV or higher, they were well correlated along the machine and their longitudinal wavelength substantially exceeded the mirror-to-mirror distance ($k_\parallel \leqslant 10^{-3}\,\mathrm{cm}^{-1}$). In the experiments at lower temperatures and larger mirror ratios, the measurements in the central and end cells often displayed a decreased coherency of the low-frequency fluctuations. Insufficient measurements were made to determine the nature of these fluctuations. Since these were observed at lower electron temperatures one could expect a resistive ballooning mode [78] to be relevant to these observations rather than the electrostatic trapped particle mode [83].

A typical sample of the data on azimuthal mode amplitudes obtained during an unstable decay is shown in

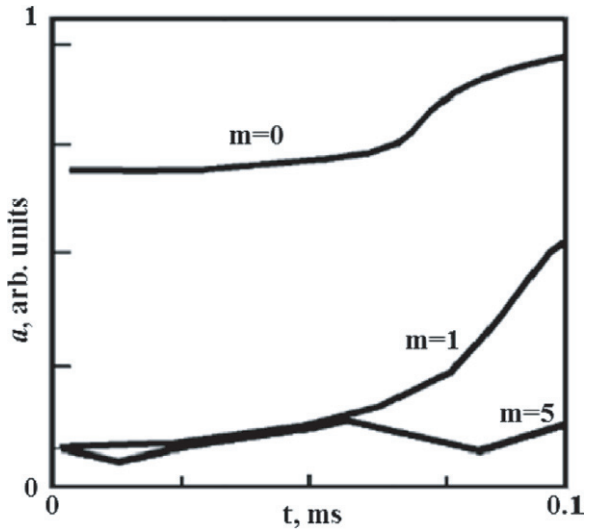

Figure 11. Time evolution of mode amplitudes.

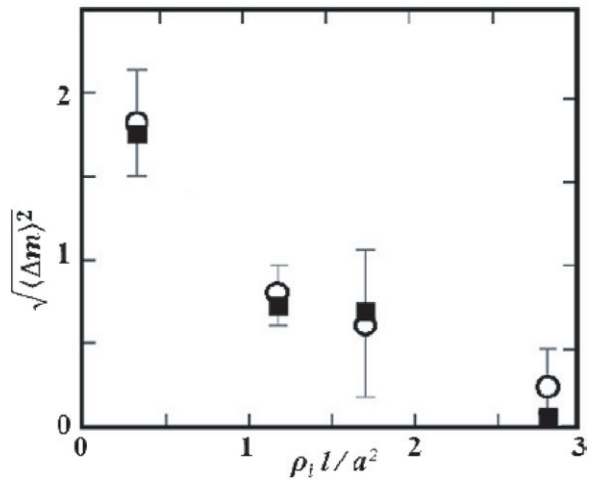

Figure 12. Width of unstable azimuthal harmonic spectra—theory (filled dots) and experiment (empty dots).

figure 11. These data were obtained without any power on the expander coils while the curvature of the field lines in the expanders was negligible, thus giving an unfavorable averaged pressure-weighted curvature in the entire trap. It was observed that growth rates of the azimuthal harmonics were different for different averaged curvatures and ion temperatures in the trap. A change of the averaged curvature was performed using a separate coil with 16 cm radius located inside the central cell. When energized, this coil strongly increased the local curvature. This increase resulted in a considerable broadening of the unstable spectra. The same alteration of the mode spectra was achieved when we switched off one of the central cell coils. The former approach turned out to be preferable because in this case the paraxial limit provided a better fit for the geometry of the field lines allowing a more relevant comparison of the data with existing theory. The averaged ion Larmor radius and ion pressure were varied by application of auxiliary ICRF heating in the central cell. For ion-cyclotron heating, we used a slot antenna [18] located at $z = 235$ cm in a position with mirror ratio $R = 3$. Absorbed power of about 50 kW for $\sim$1 ms was sufficient to increase the ion transverse pressure a few times without a change in the plasma radius, density or electron temperature. The use of ICRH was a rather suitable method to vary the averaged ion Larmor radius and ion pressure in the central solenoid. The pressure-weighted curvature was varied along with the frequency of the heating and the magnitude of the magnetic field in the trap. In particular, when the resonance zone was located near the mid-plane, where the unfavorable curvature attains its maximum, the result was a considerable increase in the calculated unfavorable curvature in the central cell. The axial pressure profile of the heated bulk ions with strong anisotropy was measured by making use of diamagnetic loops. By changing the averaged curvature of the field lines and transverse ion pressure by the application of ICRH, we were able to observe the transition from the regime with a relatively wide spectrum of unstable modes to regimes where the rigid shift mode $m = 1$ strongly dominates. These data reasonably correlate with the theory that includes finite Larmor radius (FLR) terms and considers the existence of a conductive radial limiter. In these experiments, the influence of the limiter on characteristics of the flute modes was significant, as we used a limiter of 11 cm inner radius that was comparable to the plasma radius. Figure 12 shows the dependence of spectral width on the effective $\rho_i l/a^2$ parameter (ρ_i is the ion Larmor radius, l and a are the plasma length and radius, respectively) that determines the significance of FLR effects [84, 85]. Experimentally measured growth rates agree rather well with the values calculated using the theory that includes the FLR effect. More details about these measurements and a quantitative comparison of the measured growth rates with the theory can be found in [84].

The experiments described above demonstrated successful stabilization (which was set up by the expander end cells) of the flute instability of a relatively cold collisional plasma in the long axisymmetric gas-dynamic trap. Further experiments were performed with the application of NBI into the central solenoid. The difference between these and the experiments without injection of the beams is twofold. Accumulation of anisotropic fast ions and subsequent heating of the bulk plasma electrons emphasize the FLR effects, which strongly modify the small-scale mode stability, so that ideal MHD approximation is not valid anymore. Therefore, in the comparison of the observed stability limit with the theory, we applied an energy principle that takes the kinetic effects into proper account [51]. Since only large-scale modes survive under the influence of strong FLR effects, we assumed that the stability boundary would be determined by the most dangerous $m = 1$ mode. Another difference relates to finite beta effects, which became significant with increases in the heating power and extensions of the injection pulse.

In experiments without neutral beam heating [79], the measured stabilizing contribution of expanders to equation (1) exceeds the destabilizing contribution from the central solenoid by approximately 3 times (for $R_m = 25$ and $T_e \sim 5$ eV). At the same time, these experiments revealed a disadvantage of this stabilizer, which was presumably caused by a strong reduction in the magnetic field toward the end wall. As a consequence of this, the averaged curvature of

field lines in the expander is essentially determined by the small magnetic-field region near the end wall. If the magnetic field here is very small and ion energies are sufficiently high (because of acceleration in the ambipolar potential drop between the central cell and the end wall), the curvature radius would become comparable to the ion Larmor radius. If this happens, the ideal MHD approximation is not valid anymore. Therefore, one could expect that this small-field region does not contribute to the overall MHD stability. Whenever this occurs, the stabilizing contribution of the expanders is reduced. Presumably due to this effect, the experimental data [51] showed a 2–3 times smaller contribution of the expander to equation (1) compared with the theory. In experiments with neutral beam heating it was observed that with increases in the injected power and pulse duration the plasma temperature tends to saturate at a relatively small level (15–20 eV). This indicates a transition to an unstable regime. This observation initiated the interest in alternative MHD anchors with a larger stabilizing property, which could be envisaged for use in a technically and economically viable NS.

A magnetic cusp would be a good candidate for the purpose of MHD stabilization due to a simple coil set and good MHD properties. The use of axisymmetric cusps, rather than employing simple mirror coils to plug the center cell, was described in [12]. A NS that consisted of an axisymmetric central cell bounded by a cusp anchor cell (i.e. with no plugging) was considered in [13]. MHD stability is derived from the good curvature of the cusp in combination with compressibility in the vicinity of the cusp-field null.

In the GDT cusp, the plasma outside a non-adiabatic region near the magnetic field null would be confined longitudinally in the strongly collisional regime. This contrasts with the use of cusps as end cells on tandem mirrors [86, 87] or other open confinement devices with cusp end cells such as the RFC-XX machine [88], inside of which the plasma is collisionless. The condition for this may be expressed in the form similar to equation (1): $L_{\mathrm{cusp}} \gg \lambda_{\mathrm{ii}} \cdot \ln(R_{\mathrm{cusp}})/R_{\mathrm{cusp}}$. Here L_{cusp} is the characteristic cusp length, λ_{ii} is the ion mean free path and $R_{\mathrm{cusp}} = H_{\mathrm{r}}/H_{\mathrm{min}}$ is the mirror ratio on the field line in a cusp (H_{r} is the field in the ring cusp, H_{min} is the minimum field on the field line). Under this condition, the plasma could readily be contained for about R_{cusp} ion transits through the cusp. That is, the plasma lifetime in the cusp would exceed that in an expander of the same length by a factor of R_{cusp}. This, in turn, leads to a corresponding increase in plasma density in the cusp end cell relative to the expander. Therefore, for the same minimum magnetic-field magnitude that is limited by the requirement of adiabaticity of ion motion, the cusp end cell would be capable of providing significantly higher safety factor values than an expander. In contrast to the expander, auxiliary plasma heating in the cusp is feasible, allowing a further increase in its stabilizing capability. In this case, instead of the adiabaticity requirement, characteristics of the heated plasma would be limited by finite beta effects that are not taken into account.

The measurement results obtained with the cusp end cell were found to be in reasonable agreement with the simulations. In these simulations, the plasma build-up and confinement in the cusp were determined by particle balance equations with collisional losses apart from a non-adiabatic region near the cusp null. For comparison of the experimentally observed stability boundary with the theory, we calculated the energy perturbation caused by the development of large-scale flute modes in the cusp. Details of these calculations can be found in [26].

Initial observation showed that the maximum electron temperature and the density of energetic ions achieved during NBI were very sensitive to the plasma pressure in the cusp end cell. When the pressure was small enough, the electron temperature appeared to be nearly constant and small ($\approx$15 eV) for injection power varied by the order of magnitude.In contrast to this, for higher pressures the central cell electron temperature significantly increased, exceeding 100 eV under optimized conditions. At the same time, the plasma beta reached about 20% near the fast ion turning points. Also note that when the pressure was small all diagnostics indicated a higher level of MHD plasma activity. This observation provided the evidence of transition across the MHD stability boundary. The plasma parameters in the central solenoid and in the cusp were measured at the stability boundary and were found to be consistent with the theoretical estimates. A more detailed description of the experiments and the theoretical model used can be found in [51].

Study of vortex plasma confinement in the GDT experiment. Further experiments aimed at studying the mechanisms of radial plasma transport of MHD stable plasmas in GDT were motivated to some extent by the results of experiments on the HIEI single mirror device [89, 90]. In these experiments, a transition from low to high radial confinement mode was observed with positive dc biasing of a limiter. HIEI had a completely axisymmetric configuration and the ponderomotive force produced by launching ICRF waves stabilized the plasma macroscopically against the flute instability. In these experiments, significant radial rotational shear was observed at the periphery, leading to suppression of the edge turbulence and related radial plasma transport. The effect observed in the experiments on the GDT device with the biasing of the radial limiter inside the central solenoid (see figure 13) appeared to be more substantial. It was observed that if the biasing voltage exceeded a certain value, at about the electron temperature, radial plasma losses appeared to be reasonably small even if the stabilizing end cells were not engaged. The effect of biasing is illustrated in figure 14, which shows a typical diamagnetic signal measured by a loop installed near the fast ion turning point. Stored plasma energy varies in time in a similar way to the diamagnetic signal. During the NBI pulse both the stored plasma energy and the diamagnetic signal increased in time as a result of plasma heating by neutral beams and fast ion build-up. Suddenly the plasma energy collapsed, presumably due to instability growth. This was expected because the pressure-weighted curvature was unfavorable. However, when an electric potential $\approx T_{\mathrm{e}}$ was applied to the radial limiter, we observed a transition from this regime with large radial plasma losses due to curvature-driven instability growth to the regime (figure 14) without

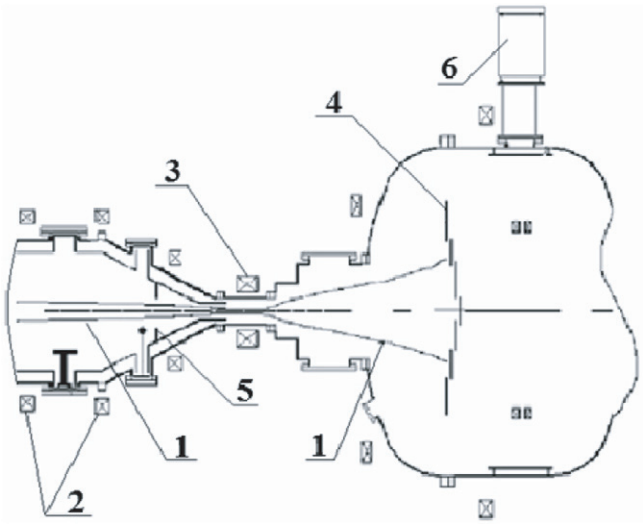

Figure 13. End tank with end plate and part of central cell of GDT device: 1—magnetic-field line, 2—coils of central solenoid, 3—mirror coil, 4—segmented plasma dump, 5—limiter, 6—pump.

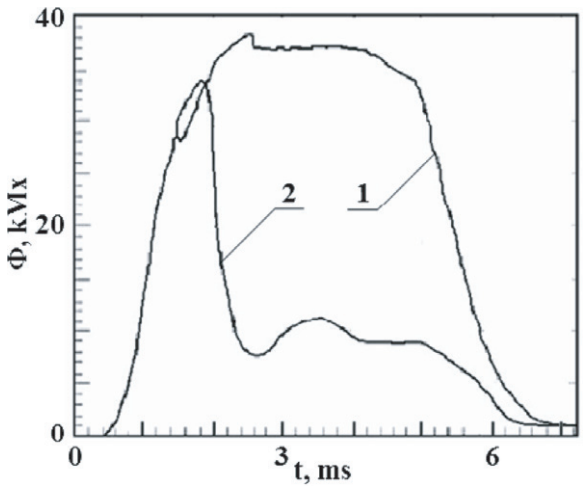

Figure 14. Plasma diamagnetism versus time: 1—with and 2—without dc bias of the limiter.

considerable radial losses. This corresponded to a maximum in plasma energy and diamagnetism. Therefore, further experiments were continued without energizing the cusp coils, so that the magnetic-field lines in the end tank were almost straight, e.g. having negligible curvature and the pressure-weighted curvature was unfavorable to stability. Plasma heating and confinement in this configuration were studied with NBI with a pulse duration extended up to 5 ms pulse, beam energies 23–24 keV, and beam power incident onto plasma in the range 3.5–5.4 MW (see table 4). Thus, the external min-B cells that provided MHD stability of the plasma in the solenoid were not engaged, and the radial plasma transport was controlled by biasing the segments of the end plate and the radial plasma limiter in the solenoid (see figure 13).

Sheared plasma rotation was predicted to stabilize unstable MHD modes. In particular, the PSP series of experiments [91] in Novosibirsk explored this technique for several years and reached ion temperatures of $\sim$10 keV at a plasma density of $\sim 10^{18}\,\mathrm{m}^{-3}$. More recently, the MCX experiment [92] at the University of Maryland has shown that stability is achieved when the shearing rate of the $E \times B$ rotation exceeds the MHD growth rate. In addition, the Gamma-10 experiment has shown that with sufficient shear (generated by end electrodes, ECH, or spontaneously) vortex structures and drift-type modes are suppressed [93]. These experiments demonstrate the important role that rotation can play as an axisymmetric stabilizer. In the experiments [94], a strong radial electric field was generated in the plasma core, which caused the whole plasma to rotate. However, if the plasma density decreases with radius, MHD theory generally predicts plasma destabilization by rotation. This excludes some specific boundary conditions for which eigenmodes of flute instability do not exist [95]. A distinctive feature of the experiments on the GDT device is shown by the concentration of the plasma rotation in a relatively narrow zone with width $\Delta r \ll a$ at the outmost plasma periphery near the edge of the biased limiter. This produces a vortex (sheared $E \times B$ flow) at the periphery. The presence of large gyro-radius ions also introduces FLR stabilization effects, so that only large-scale modes with $m \approx 1$ survive. Then, as shown in [96], the inherently unstable flute modes growing in the core would nonlinearly saturate due to the line-tying mechanism and generation of transverse currents in the vortex region. As a result, the plasma resides in the vortex interior without considerable radial excursions and losses. However, this theory cannot be directly applied to the experiments at a GDT since it assumes $\langle \rho_\mathrm{i} \rangle \ll a$ when the real experimental conditions correspond to $\langle \rho_\mathrm{i} \rangle \approx a$. So, further efforts are required to develop a more adequate theoretical explanation for the observed plasma behavior. Significance of the end wall segments and limiter biasing is illustrated by figure 15, which shows temporal variation of the plasma line density in different regimes.

The experimentally measured profile of the plasma floating potential is shown in figure 16. While obtaining these results the limiter and the outmost segment of the end plate were set to about 130 V, the other internal segments of the end plate were grounded. It is seen from figure 16 that the profile has a finite width, which is thought to be set by the development of the Kelvin–Helmholtz instability [96].

Plasma activity was monitored through measurements of the signals from the azimuthal and axial arrays of magnetic coils installed at the vacuum chamber walls. Typical waveforms of the signals corresponding to flute-like perturbations of the plasma with different azimuthal numbers are shown in figure 17.

It is seen that the mode with small azimuthal numbers dominates. This was expected by considering the significance of the effects of FLR radius. The presence of the mode with $m = 0$ is connected mainly to plasma heating during NB injection. Higher modes with $m = 3, 4$ are considerably smaller in amplitude compared with the modes with $m = 1, 2$. These are connected to plasma offset and elliptical distortion of the plasma cross section. Another observation is that during a shot, the mode amplitudes do not grow exponentially as one might expect because the magnetic-field lines have unfavorable curvature everywhere. Rather, the mode amplitudes are

Table 4. Parameters of the GDT achieved with different MHD stabilizers.

Parameter	Expander end cells [79, 80]	Cusp end cell [26]	Induced sheared plasma rotation [97]
Magnetic field at mid-plane	Up to 0.22 T	Up to 0.22 T	Up to 0.3 T
in mirrors	2.5–15 T	2.5–15 T	2.5–15 T
Bulk plasma density	$(1.5–7) \times 10^{19}$ m^{-3}	4.5×10^{19} m^{-3}	$(3–6) \times 10^{19}$ m^{-3}
Radius at the mid-plane	≈6.5 cm	5–10 cm	6–7 cm
Electron temperature	Up to 25 eV	Up to 70 eV	Up to 250 eV
Energies of deuterium/hydrogen neutral beams	15 keV	15–16 keV	24–25 keV
NB pulse duration	1.2 ms	1.2 ms	5 ms
Total injection power		Up to 4 MW	Up to 5.7 MW
Injection angle	45°	45°	45°
Fast ion density in turning point regions	$\approx 1 \times 10^{18}$ m^{-3}	$\approx 0.4 \times 10^{19}$ m^{-3}	$\approx 5 \times 10^{19}$ m^{-3}
Averaged curvature in the MHD anchor relative to that in the central cell without contribution of fast ions	1.5–2	≈8 for $R = 25$	
Mean energy of fast ions		5–8 keV	≈10 keV
Maximal local plasma ß	≈0.07	≈0.1	Up to 0.6

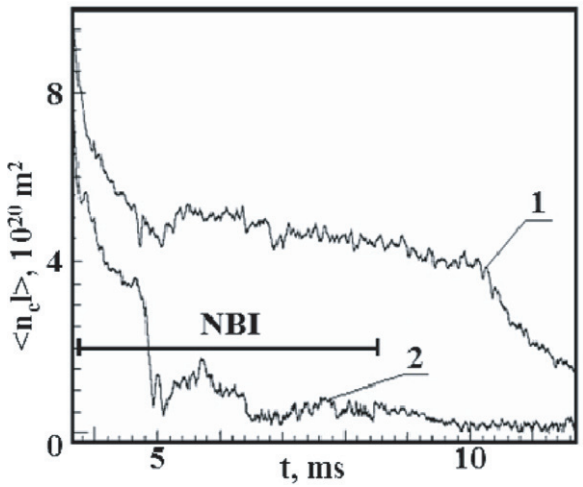

Figure 15. Plasma line density versus time: 1—with and 2—without dc bias of the limiter.

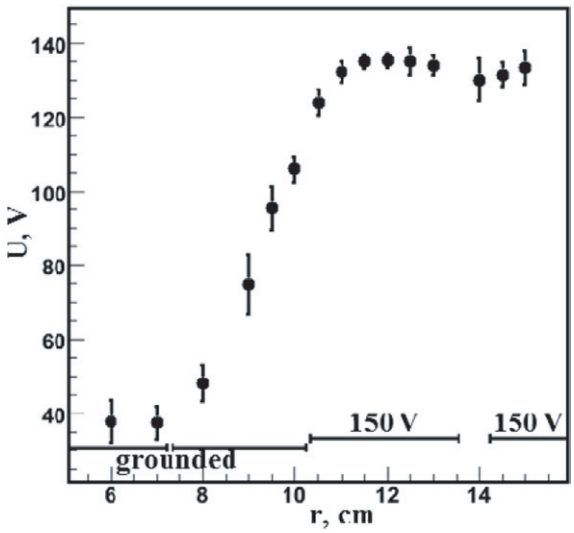

Figure 16. Profile of floating plasma potential (dots). Bottom of the chart shows regions corresponding to the limiter and sections of plasma dump.

limited indicating that the sheared plasma rotation at the periphery precluded from non-limited growth of the flute-like perturbations. An interesting feature of the amplitudes' behavior is the significance of the $m = 2$ mode, which almost always has a several times larger amplitude than the $m = 1$ mode. Note that the mode with $m = 1$ is predicted by a linear theory to have a higher growth rate. Therefore, the transition to the dominance of the $m = 2$ mode in the course of time might indicate a considerable role of non-linear mechanisms [96]. The frequency spectra of the modes with $m = 1, 2$ were found to be quite wide, and their maxima lay in the range 15–50 kHz. Both modes have approximately the same frequency, which began at about 40 kHz and subsequently dropped down to ∼20 kHz or lower frequency at about 2 ms after the start of NBI. For the shot which is represented by figure 17, this frequency drop from ∼40 to ∼20 kHz occurred at about 5.7 ms when the amplitude of the $m = 2$ mode increased stepwise and became larger than that of the $m = 1$ mode.

It is worthwhile to compare the measured frequencies of the observed flute-like perturbations with the characteristic growth rate of MHD instability and plasma rotation frequency in this case. The growth rate of an unstable flute mode in a field with unfavorable curvature, as in the GDT with the stabilizing end cell not engaged, can be estimated to be on the order of $\gamma \approx \omega = 2\pi f \approx V_{T_i}/(a|R|)^{1/2} \approx V_{T_i}/L$. This represents a rate given by the ion thermal speed V_{T_i} divided by the length of the plasma L. For the current GDT experiments, the ion speed can be estimated by assuming the ion mean energy to be 10 keV and by taking $L \approx 6–7$ m, which gives $f_{\mathrm{MHD}} \approx 30$ kHz. The plasma rotation frequency is determined by a drift velocity $V_{\mathrm{drift}} = cE/H$ and the plasma radius $a \approx 10$ cm. Taking $E = 30–50$ V cm^{-1}, which corresponds to the potential profile shown in figure 16, we obtain $f_{\mathrm{rotation}} \approx 15–30$ kHz. These estimates are quite close to the perturbation frequencies observed in the experiments (15–50 kHz). Since the rotation frequency is quite close to the estimated frequency and growth rate of the flute instability, one can conclude that the plasma rotation would have a significant effect in these experiments.

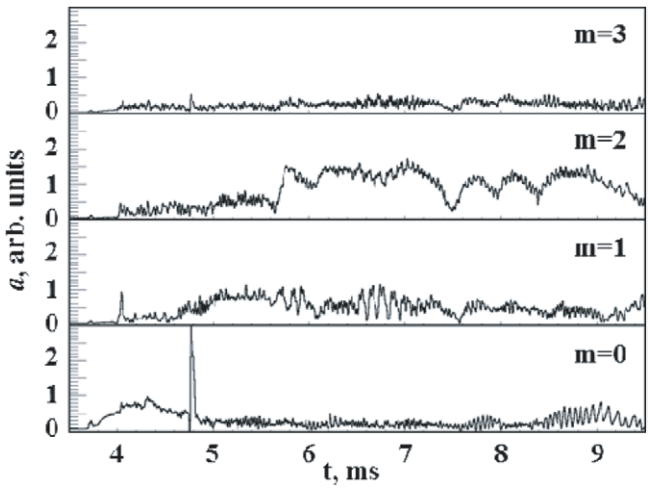

Figure 17. Amplitude of flute-like perturbations with different azimuthal numbers versus time. NB injection started at 3.7–4 ms.

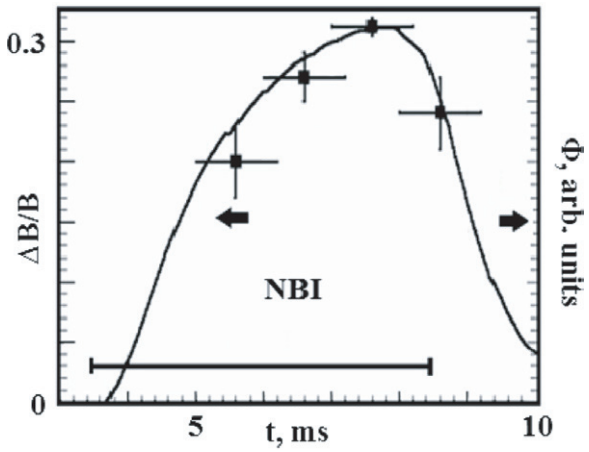

Figure 18. Magnetic-field depression (dots) and local plasma diamagnetism (line) versus time.

The stored plasma energy in the regime with sheared plasma rotation at the periphery increases, as shown in figure 18, during the entire duration of beam injection. Thus, one can conclude that the transverse energy losses are quite negligible in the plasma-energy balance. The density of the fast ions with a mean energy of 10–12 keV reached $\approx 5 \times 10^{19}$ m^{-3} in the turning point regions and substantially exceeded that of the target plasma ($(1.5\text{–}3) \times 10^{19}$ m^{-3} at the mid-plane). This resulted in the development of peaks of the ambipolar potential and a considerable reduction in plasma axial losses in the region near the plasma axis.

The local plasma beta in the turning point region was determined from a MSE diagnostic. Relative to the vacuum field the local depression of the magnetic field reaches about 0.35 (see figure 18), i.e. the plasma beta reaches about 0.6.

The radial profile of $\Delta B/B$ mapped onto the mid-plane of the GDT is shown in figure 19 along with the plasma density profile in [98]. These data were taken in a series of shots with the magnetic field at the mid-plane at 0.25 T. According to the data presented in figure 19, the magnetic-field depletion amounts to $\geqslant 0.2$ on the plasma axis. It allows for the conclusion that the perpendicular plasma β under these

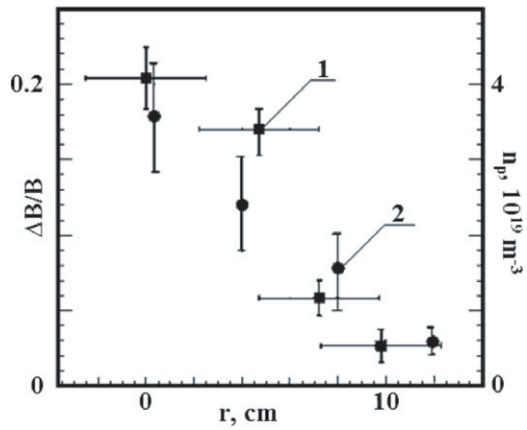

Figure 19. Radial profiles: 1—magnetic-field depletion, 2—plasma density.

experimental conditions exceeds 0.4. The distinctive feature of the radial profile is its quite small width. It amounts to about 7 cm at the $1/e$ level mapped onto the GDT mid-plane. This is only slightly larger than the fast deuteron gyro-radius ($\rho_i \approx 5.6$ cm) calculated for the magnetic field of 0.25 T and for 10 keV, an energy that is close to the fast ion mean energy.

Note that according to the measured axial profiles of the fast ions and target plasma parameters [98] the total plasma beta exhibits only slight 30–40% variations within the 3.8 m between the fast ion turning points. Beyond the turning points the plasma beta drops down very significantly.

A study of the plasma-energy balance with NBI has shown that the high-beta plasma in the GDT experiment does not exhibit any indication of increased transverse losses for the maximum plasma beta reached so far ($\beta = 0.6$) [97].

However, at plasma beta exceeding $\approx$0.4, some plasma perturbations appeared, which can be divided into two categories: relatively slow with a frequency of about 10 kHz and relatively fast with frequency in the MHz range. An example of the low-frequency perturbation is a spontaneous redistribution of plasma pressure along the central solenoid and distortions of plasma shape in the transverse cross section. These effects were observed in some high-beta shots [99]. In these cases, plasma behavior is illustrated in figures 20 and 21. Figure 20 shows signals from diamagnetic loops installed at the mid-plane (mirror ratio $R = 1$) and at the turning point of fast ions (mirror ratio $R = 2$). In this shot, as plasma beta rose, the signal from the loop installed near the fast ion turning point dropped considerably between 4.1 and 4.2 ms. At the same time, the axial profile of magnetic-field disturbance measured by the magnetic probes changed considerably, indicating a broadening of the plasma pressure profile along the device.

Another example of spontaneous low-frequency perturbation of a high-beta plasma in the GDT is shown in figure 21, which shows signals from the neutral beam attenuation detectors in a high-performance shot with beta close to 0.6. It can be seen that at some moment all the signals started to oscillate with high amplitude, indicating an elliptical distortion of the plasma cross section and an azimuthal rotation of the plasma column. Note that during these events no considerable plasma losses were measured along the magnetic field or in the transverse direction. It is believed that these would occur above a

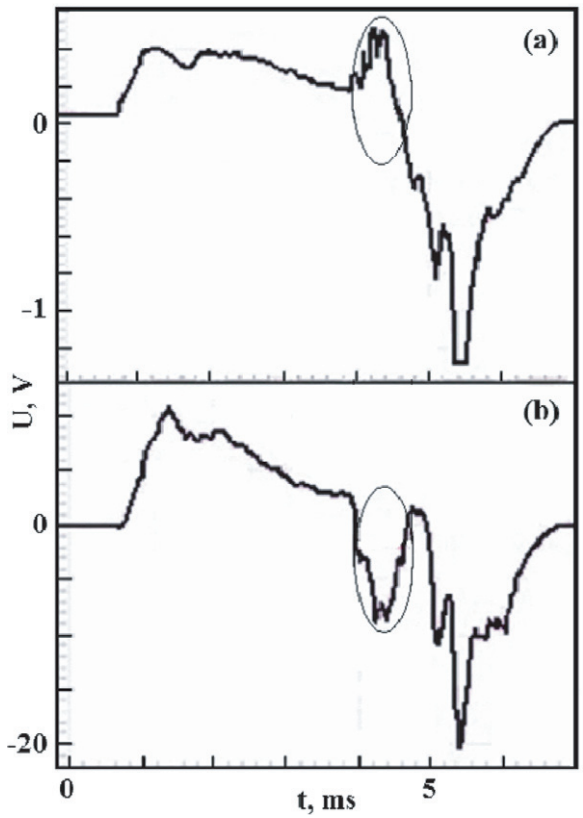

Figure 20. Signals from diamagnetic loops versus time: (*a*) at the mid-plane and (*b*) at the fast ions turning point.

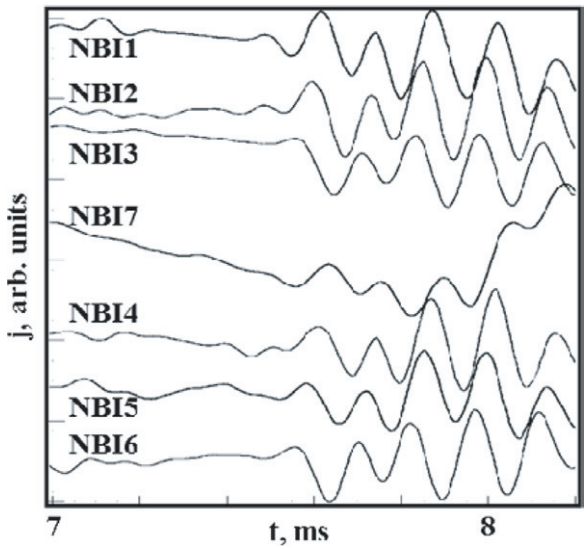

Figure 21. Signals from attenuation beam detectors.

plasma beta of about 0.6, which in accordance with this theory is a threshold for plasma ballooning.

With an increase in injection power, plasma diamagnetism exhibited several 'saw-teeth' relaxations (see figure 22(*b*)) that were accompanied by bursts of RF noise at a characteristic frequency of about 1 MHz. As seen from figure 22(*b*), intervals between the relaxations become shorter as the plasma pressure rises. Measurements of the characteristics of the fast plasma perturbations, which appear in these saw-teeth relaxations, show that they are similar to Alfvén ion-cyclotron electromagnetic waves that could become unstable at a sufficiently high plasma beta. A discussion of these results, as well as possible theoretical explanations, is presented below in section 5. Additional measurements are still required in order to establish a correlation of these events with an increase in plasma beta and other plasma parameters. Nevertheless, the observed phenomena indicate that the plasma in the GDT approaches a beta threshold. This might be a factor preventing further increase in the plasma parameters in the GDT experiment.

5. Fast ion relaxation and confinement

One of the key features of the GDT-based NS is the presence of fast sloshing ions, the effects of which were first examined theoretically in [100]. These ions have a spatially skewed distribution function created principally by angled NBI. 'Sloshing' refers to the axial bouncing motion of ions within the confining magnetic field. The ions spend more time near their turning point, where they axially move more slowly than they do at the solenoid mid-plane. This peaks the fast ion density and pressure, as well as the neutron reaction yield near the turning points, in contrast to a conventional mirror plasma distribution that peaks at the mid-plane. At the same time, the sloshing-ion distribution provides better ion micro-stability. In particular, it is true near the turning points where the sloshing-ion distribution is practically isotropic. After upgrade of the GDT neutral beams [97], six or in some experiments eight beams inject sloshing ions into the solenoid of the GDT delivering up to 5.4 MW of power. The trapped ions remain peaked near their injection angle of 45° to the magnetic-field lines. The fast ion density varies up to $5 \times 10^{19}\,\mathrm{m}^{-3}$ in the turning points and the lifetime varies between 0.1 and about 3 ms, depending on the experimental conditions. The mean ion energy is about 10 keV in high-performance shots. The ions are localized within a 14 cm radial extent projected at the mid-plane and a 4 m length. A density at the turning points ($B \approx 6$ kGs) of approximately thrice the mid-plane ($B \approx 3$ kGs) density is evaluated.

This section presents the results of experimental and numerical studies of fast ion relaxation and confinement in the GDT. A comparison of the experimental results with the data obtained with numerical simulations allowed us to demonstrate that sloshing ions remain peaked near the injection angle, thereby producing fast ion density peaked off the solenoid mid-plane, and that their angular spreading and slowing down are determined by classical Coulomb collisions. The ion distribution function was calculated using a bounce-averaged one-dimensional Fokker–Planck model (FPM) and Monte Carlo (named FIT) codes [101, 102] with input parameters derived from numerical simulations of the warm plasma parameters, which were performed using a set of equations including gas-dynamic particle and energy losses through the ends, temperature exchange between the bulk plasma electrons and ions, and electron heating introduced by the fast ions [2]. The spatial and temporal evolutions of the neutral gas during a shot were calculated using Monte Carlo codes [102]. The

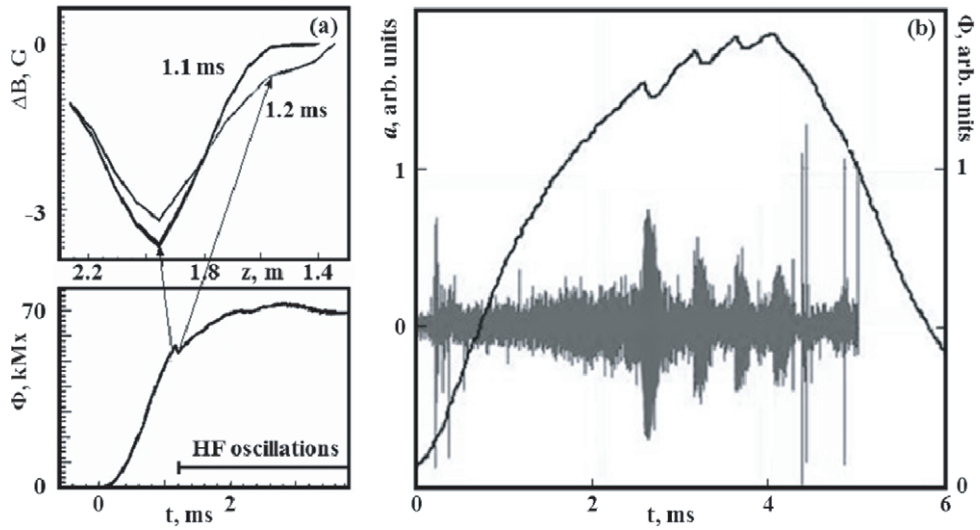

Figure 22. (*a*) Axial broadening of fast ion reflection region; (*b*) saw-teeth relaxations during fast ion density/pressure build-up.

major sources of the neutral gas were a gas puff from the beam lines of the injection system and plasma recombination on the radial limiters inside the central solenoid of the GDT.

Below we will present the results of a detailed comparison of the results of numerical simulations and experimental data [103], which was performed for the regime of GDT with duration of NB injection pulse of 1 ms, when the electron temperature reached about 100 eV and plasma beta was in the range 0.1–0.2. The plasma was stabilized by the cusp end cell attached at one end of the central solenoid, whereas at the opposite end an expander end cell was attached. The injection energies for different beams in these experiments were in the range 12.5–17.5 keV. All the conclusions about fast ion relaxation and confinement for this particular regime remain valid for the regimes with longer 5 ms beams and higher electron temperatures.

Figure 23(*a*) illustrates the global energy balance of the fast ions in this regime. The total power $P_{\rm inj}$ injected by the neutral beams was inferred from the ion current and acceleration voltage data of each injector considering their measured neutralization efficiencies, which vary in the range 0.82–0.85 for different injectors according to the data given in table 3. The trapped power $P_{\rm tr}$ was then experimentally determined using the beam attenuation measurements. The fast ion energy content $W_{\rm F}$ was measured by the diamagnetic loops and the power of the charge-exchange losses $P_{\rm ex}$ was measured by an array of pyro-bolometers. Subsequently, the electron drag power $P_{\rm Fe}$ was evaluated using the energy balance equation, which does not account for the direct radial losses of the fast ions to the limiters and their axial losses through the mirrors. Both of these effects are considered to be negligible compared with the other terms in the energy balance equation

$$P_{\rm Fe} = P_{\rm tr} - \frac{{\rm d}W_{\rm F}}{{\rm d}t} - P_{\rm ex}$$

In figure 24 we compare measurements of fast ion energy content with results from the Fokker–Planck and Monte Carlo codes. Considering the accuracy of the experimental

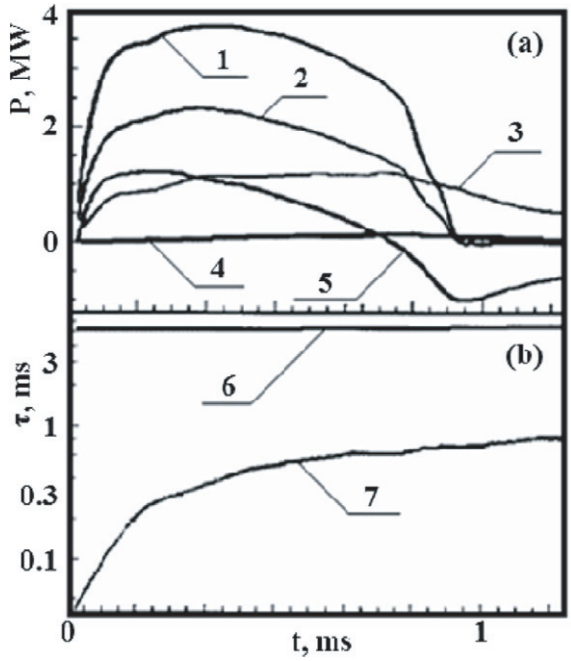

Figure 23. Fast ion power balance data (*a*) and characteristic times (*b*) in 1 ms neutral beam pulse: 1—$P_{\rm inj}$, 2—$P_{\rm tr}$, 3—$P_{\rm Fe}$, 4—$P_{\rm ex}$, 5—${\rm d}W_{\rm F}/{\rm d}t$, 6—charge-exchange time, 7—electron drag time.

data (about 15%) one can see a quite good agreement. This indicates that the fast ion energy relaxation rate in the warm plasma background is dominated essentially by Coulomb collisions with the bulk plasma particles and by charge exchange with the neutral gas. Note that the charge-exchange losses did not significantly contribute to the fast ion energy balance in the regime under consideration, shown by figure 23(*a*).

The times of electron drag $\tau_{\rm Fe}$and charge exchange $\tau_{\rm ex}$ (global characteristic) of fast ions are depicted in figure 23(*b*). They were calculated using the energy balance data through the following relationships: $\tau_{\rm Fe} = W_{\rm F}/P_{\rm Fe}$; $\tau_{\rm ex} = W_{\rm F}/P_{\rm ex}$.

Initially, when the neutral beams started up, the electron drag time was several tens of microseconds only. Later,

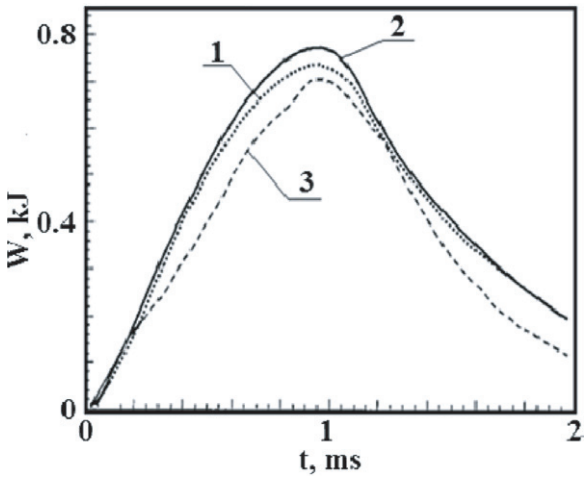

Figure 24. Fast ion energy content versus time with 1 ms NB injection: 1—MC FIT calculation (Monte Carlo), 2—FPM calculation (kinetic), 3—experiment.

the electron temperature increased up to 100 eV in these experiments, causing the electron drag time to rise to ∼0.8 ms (at the highest electron temperatures achieved so far it is about 3 ms). Note that in our case, the value of the electron drag time was close to the total energy confinement time of fast ions. The charge-exchange losses were measured and found to be considerably small during NBI ($\tau_{ex} \sim 10$ ms).

In order to double check the drag time τ_{Fe}, a special experiment was carried out. The DNB installed near the mid-plane served as a source for the build-up of fast test ions. They were injected at 0.61–0.74 ms after the start of the main neutral beams. Since the DNB was not directed exactly along the radius, but under a pitch angle of 85°, the resulting test ions were sloshing within an ∼100 cm long region near the GDT mid-plane. Because of their different pitch angles, the fast test ions could be experimentally separated from the main fast ions. Note that the energy of DNB particles (13.6 keV) was close to the energy of the main neutral beams (12.5–17.5 keV) in these experiments. Figure 25(*a*), which presents the time evolution of the neutral fluxes to different channels of the energy analyzer, demonstrates the dynamics of test ion relaxation. The energy distributions of the test charge-exchange particles at different time points are shown in figure 26. The global time of energy losses of test ions in the given background was calculated using the temporal behavior of the test ion mean energy. At 0.65–1.0 ms after the start of the main neutral beams the measured energy relaxation time was about 0.7 ms, as shown in figure 25(*b*). This value is close to the value determined through the analysis of the global energy balance for the main hot ion population (figure 23(*b*)).

The measured energy distributions of fast ions exhibit the kinetics of energy transfer from the hot ion population to the bulk plasma. This may be assumed to be more sensitive to possible anomalies in the fast ion relaxation than global parameters. The fast ion energy and angular distributions were inferred from the energy spectrum of charge-exchange particles. In accordance with the results of [103], the major

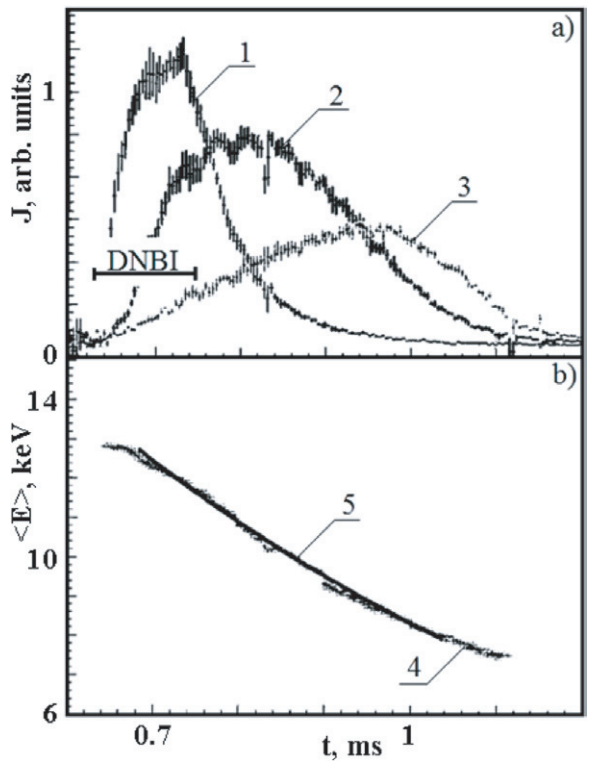

Figure 25. (*a*) Time evolution of the fluxes of test charge-exchange neutral particles: 1—13.6 keV, 2—10.1 keV, 3—7.4 keV. (*b*) Mean energy of the test ion population versus time: 4—experimental data, 5—fit with drag time $\tau = 0.75 \pm 0.04$ ms.

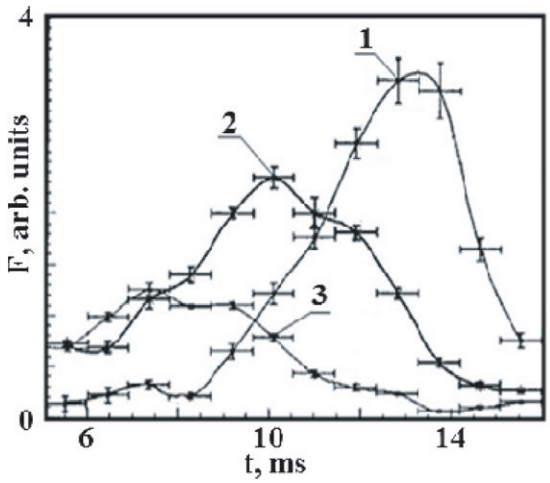

Figure 26. Test ion distribution over energies: 1—0.7 ms, 2—0.85 ms and 3—1.0 ms after injection of test ions.

sources of the charge-exchange neutrals in the GDT are interactions of the fast ions as follows:

- with the cold peripheral neutral gas, which includes residual gas and neutrals from plasma limiters;
- with the warm neutral atoms, which are generated by charge exchange of the main neutral beams with the warm ions of the target plasma;
- with the main neutral beams;
- with the artificial charge-exchange target produced by the separate DNB.

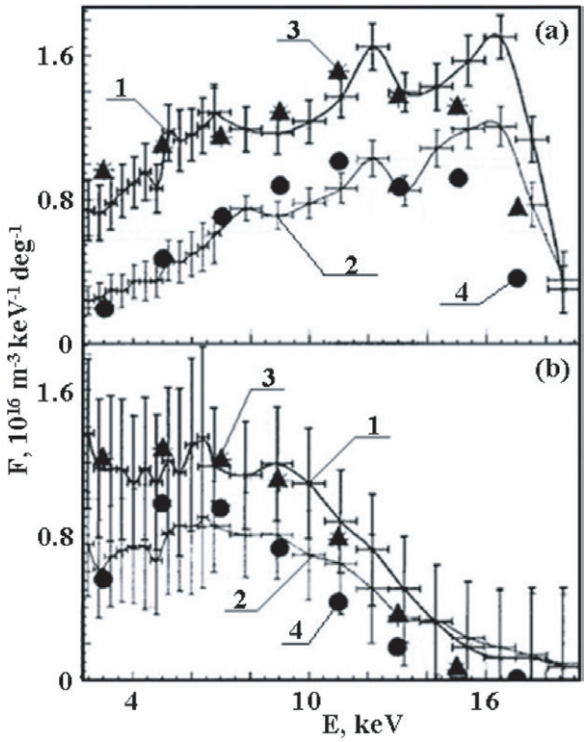

Figure 27. Local energy distribution functions of the fast ions in the range of pitch angles $45 \pm 0.35°$: (*a*) at 0.625 0.725 ms and (*b*) at 1.225 1.325 ms after the start of NBI. Curves 1 and 2 represents the measurements in the radial intervals 0–4 cm and 6.5–10.5 cm respectively. Dots 3 and 4 show the results of MC FIT calculation for these positions.

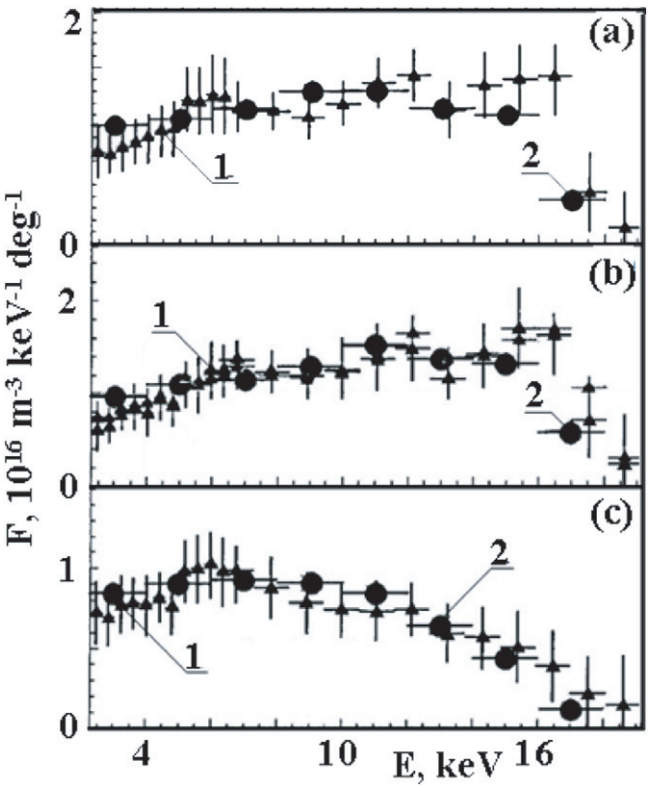

Figure 28. Energy distribution functions of fast ions for a pitch angle of 47° (*a*), 45° (*b*) and 42° (*c*) at 0.625 0.725 ms after the start of NBI: 1—experimental data at the axis, 2—results of MC FIT calculations.

In contrast to the first three sets of interactions, the artificial target enables one to measure the local energy distributions with a reasonable spatial resolution. In figure 27, the local energy distribution functions of the fast ions at the vertical mid-plane of the GDT are presented at different points in time after the NBI start, for a near-axis region and for a radius of about 8.5 cm. The distribution functions were measured with a spatial resolution of 4 cm for a pitch angle interval of $45 \pm 0.35°$.The energy analyzer and diagnostic beam injector were located near the mid-plane. For comparison, the results of the FIT code simulation are also shown. As seen in figure 27, at the stage of NBI (0.6–0.7 ms) the maximum of the distribution function is close to the NBI energy. The depletion of low-energy particles is explained, in this case, by the ion angular scattering.

The data from the plasma periphery exhibit a relatively smaller number of particles in the energy range 3–6 keV. A reasonable explanation of this fact is that the ratio of electron drag time to charge-exchange time at the plasma periphery is larger compared with that in the plasma core. Therefore, at the periphery, fast ions are lost with a higher probability before they slow down to the low-energy range.

The fast ion near-axis energy distributions for pitch angles 40°–48° were also measured. In this case, the available range of pivoting angles of the CXA and the DNB limited the pitch angle interval. The distributions for other pitch angles were measured by the CXA being shifted to different positions along the machine axis. The view line of the energy analyzer at these positions was perpendicular to the axis, allowing the measurement of the energy distribution function of the fast ions whose turning points were close to the CXA location. The corresponding pitch angles mapped onto the mid-plane were 46.7°, 38.2° and 31.7° each with an angular resolution of ∼1°.

The fast neutrals result from the fast ion charge exchange with the background neutrals. The injection of the DNB to produce the artificial target was not effective here due to problems with separation of the charge-exchange flux from the main population of fast ions, as well as the additional population produced by the trapped DNB particles. The energy distribution functions for a set of pitch angles at 0.625–0.725 ms after the start of NBI are shown in figures 28 and 29. The difference in the measured and calculated energy distributions at 31.7° for high (8–18 keV) energies can be explained by the presence of a small fast ion fraction with a large angular spread (figure 29(*c*)), which results from the neutral beam halo particles with large angular divergence. The number of ions with a large angular spread was estimated to be ∼3–5% of the entire population.

The fast ion angular distributions were inferred from the energy spectrum measurements at different pitch angles. Experimentally measured and modeled angular distributions for a set of energy intervals are shown in figure 30. Note that the angular spread at high energies (14–18 keV) is close to that in the injected neutral beams. The angular spread of the ions with energies 3–5 keV was approximately three times larger than

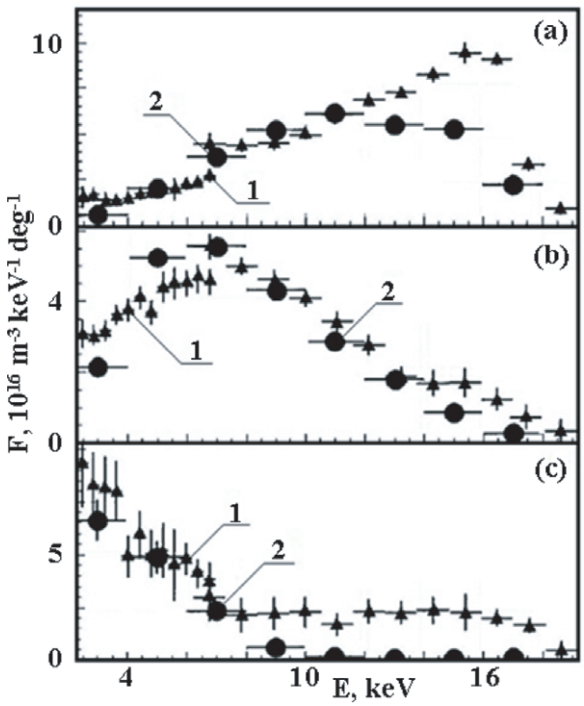

Figure 29. Energy distribution functions of fast ions for a pitch angle of 47° (*a*), 38° (*b*) and 32° (*c*) at 0.6–0.9 ms after the start of NBI: 1—experimental data at the periphery, 2—results of MC FIT calculation.

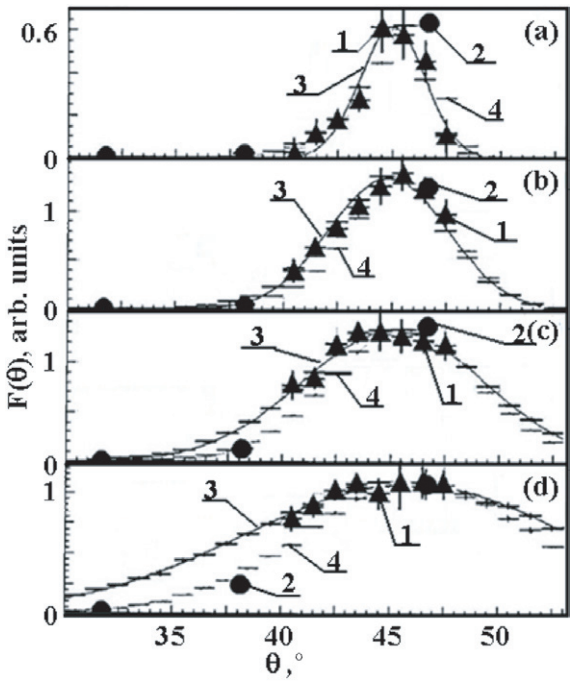

Figure 30. Angular distribution of fast ions for energy interval of 16–18 keV (*a*), 12–14 keV (*b*), 8–10 keV (*c*) and 4–6 keV (*d*) at 0.6–0.9 ms after the start of NBI: 1 and 2—experimental data at the axis and on the periphery; 3 and 4—results of MC FIT calculations for these positions.

that for the injection energy. The angular spread ($\Delta\theta$) gained for the ions with current energy E_i can be estimated from a relationship that follows from the Fokker–Planck equation for an ion beam, which is slowed down and scattered by a given uniform background plasma [103]:

$$\Delta\theta^2(E) = \Delta\theta_0^2 + \frac{3}{2}\sqrt{\pi\frac{m_i}{m_e}}\left(\frac{T_e}{E_i}\right)^{3/2}\left(1-\sqrt{\frac{E_i}{E_0}}\right),$$

where E_0 and $\Delta\theta_0$ are the energy and angular spreads of neutrals in the injected neutral beams, respectively. The experimental data and estimated values of the fast ion angular spread for the given experimental conditions are presented in figure 31 as functions of ion energy. The results refer to a time interval of 0.6–0.8 ms after the NBI start when the electron temperature was ~70 eV. From this picture one can conclude that the measured angular spread of the ions is explained quite well by their Coulomb interaction with the bulk plasma particles. From this observation, it can be further concluded that within the measurement accuracy microinstabilities that could cause significant additional scattering of fast ions have not yet been observed. Nevertheless, more recent data obtained at higher plasma parameters when the neutral beam duration was extended to 5 ms indicate the presence of sloshing-ion instability, which, however, does not considerably change the fast ion distribution except of a relatively small fraction of ions resonant with the wave. This observation is discussed below in this section.

The global energy distribution functions of the fast ions obtained through the integration of experimentally measured functions over pitch angles and spatial co-ordinates are shown

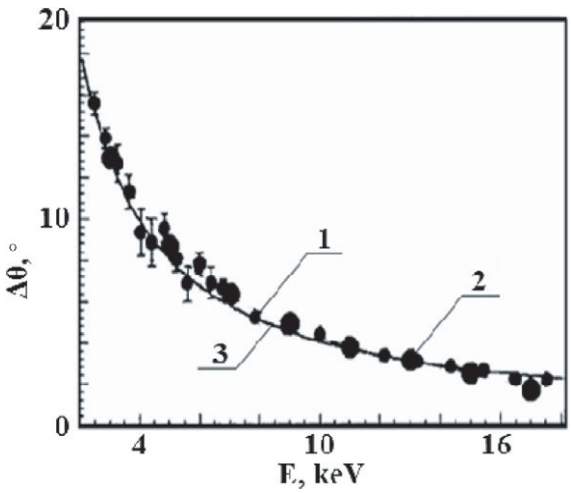

Figure 31. Angular spread of fast ions versus energy at 0.6 0.9 ms after the start of NBI: 1—experiment, 2—MC FIT calculation, 3—analytic estimate.

in figure 32 for time intervals during and after NBI. It is seen that the distribution evolves over time, causing ions to accumulate in the low-energy range. One would expect this provided the dominant process is speed reduction without significant particle losses. One can determine the mean energy of the ions through the integration of the global energy distribution functions. For example, this mean energy was estimated to be 8.5 keV for the time interval 0.6–0.9 ms, which corresponds to the maximum of the fast ion density and β.

Fast ion density profiles. The radial sloshing-ion density profile is determined with a number of diagnostics including

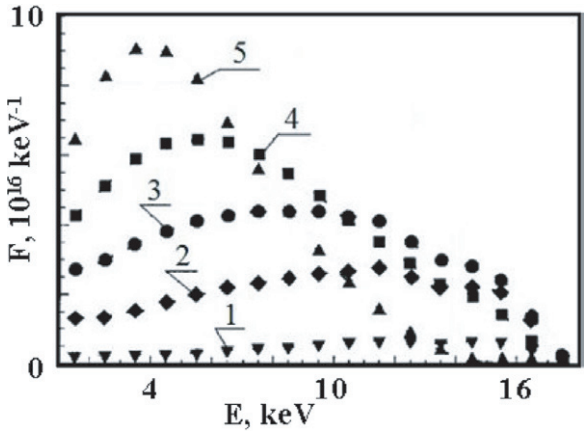

Figure 32. Global energy distribution functions: 1—0–0.3 ms, 2—0.3–0.6 ms, 3—0.6–0.9 ms, 4—0.9–1.2 ms and 5—1.2–1.5 ms after the start of NBI.

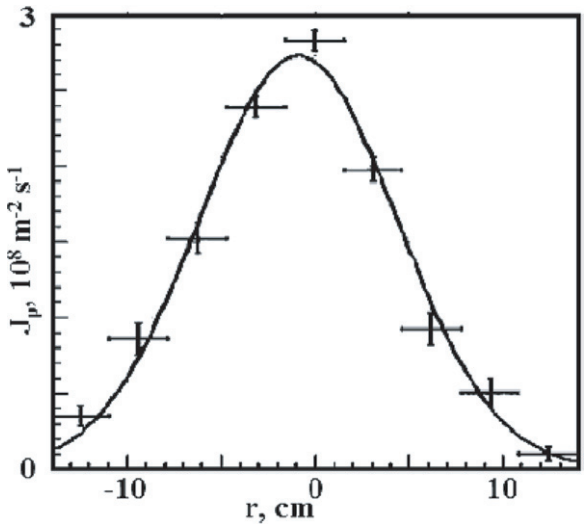

Figure 33. Radial profile of fusion proton yield: dots—experiment, curve—Gaussian fit with the width at half-maximum of $d = 12$ cm.

active charge-exchange, spatially resolved fusion product measurement and MSE measurements of the field depletion at the turning point, which is mainly determined by their pressure profile. Figure 33 shows a plot of the radial data from a DD fusion proton detector [104]. The profile is rather narrow, which also indicates that the fast ion density profile is narrow.

This observation was confirmed by measurements of the charge-exchange neutrals from the plasma (figure 34). Radial profiles of the neutral flux were obtained by the neutral particle analyzer [105] similar to that described in section 3 (see figure 7). It is seen that the CX profiles are shifted left by approximately the Larmor radius of the fast ions. Profile width at half-maximum is less than 10 cm for particles with energies 16 keV and lower. The profile of charge-exchange neutrals at energies close to the injection energy (20 keV in figure 34) is 1.5 times wider and reasonably agree with the results of numerical simulations of neutral beam trapping and further motion of the fast ions in the warm plasma. The mechanism that causes the formation of the narrow radial profile of fast ions is still not clear enough, but it should be noted that this is not a result of enhanced losses of fast ions

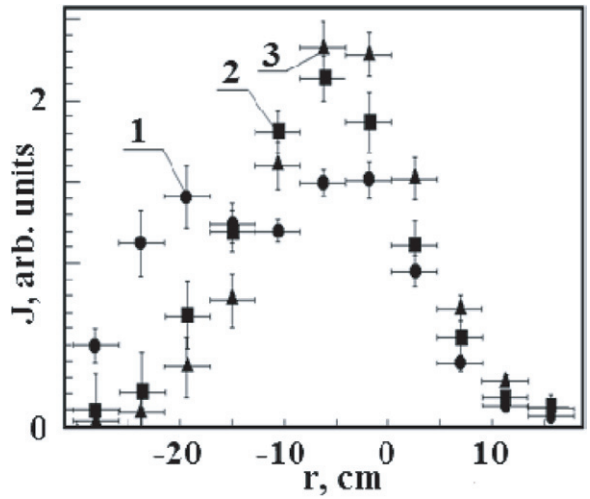

Figure 34. Radial profiles of charge-exchange flux: 1—20 keV, 2—16 keV and 3—13 keV particles.

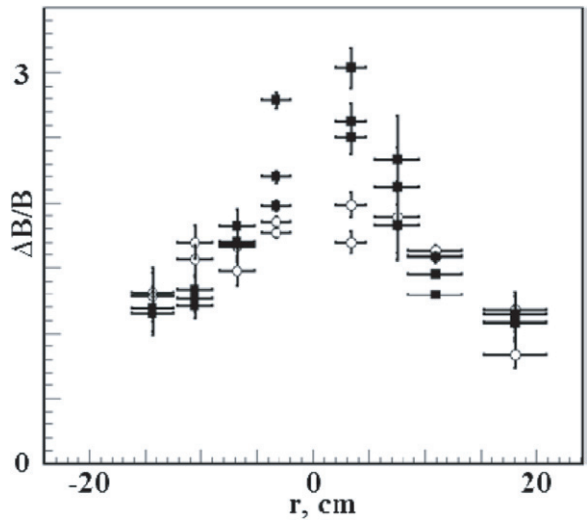

Figure 35. Profiles of the magnetic-field depletion for positive (filled circles) and negative (open circles) limiter bias at the periphery.

at the periphery [105]. An additional insight into the problem provides the experiments with reversed plasma rotation at the periphery. Then, the plasma also resides inside the region of the reversed vortex resembling small cross-field transport, but the radial profile of the fast ion density is considerably wider in this case, thus indicating the role of plasma rotation on the formation of the fast ion density profile. The effect of the rotation direction on the radial transport of the fast ions is illustrated in figure 35, which shows the magnetic-field depletion for shots with positive and negative limiter bias that produces left-hand and right-hand rotation.

The measurements indicate that the fast ions have a relatively narrow angular spread. Therefore, the longitudinal fast ion density profile is peaked near the turning points. This circumstance is very important for the GDT-based NS [3, 4]. To experimentally prove this peaking effect, special measurements of DD fusion products were carried out [106]. Deuterium neutral beams with the energy 13–17 keV and total

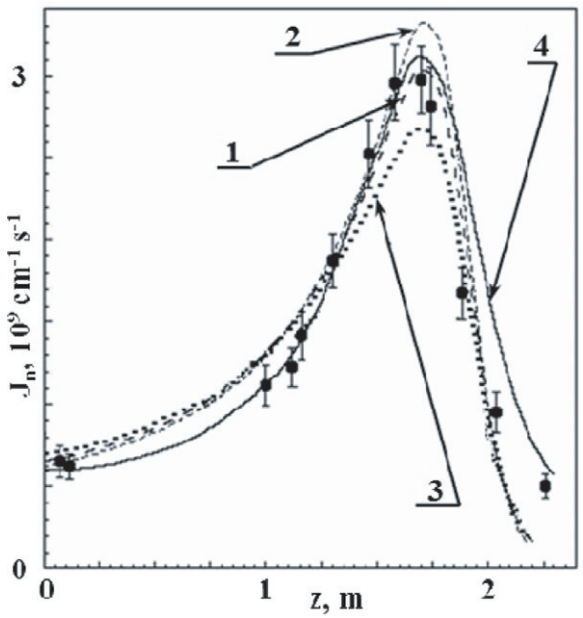

Figure 36. Axial profile of DD reaction yield as measured from the mid-plane ($z = 0$): dots—experiment, 1—analytical, normal scattering, 2—analytical, 25% reduced scattering, 3—analytical, 25% enhanced scattering, 4—calculated by MC FIT.

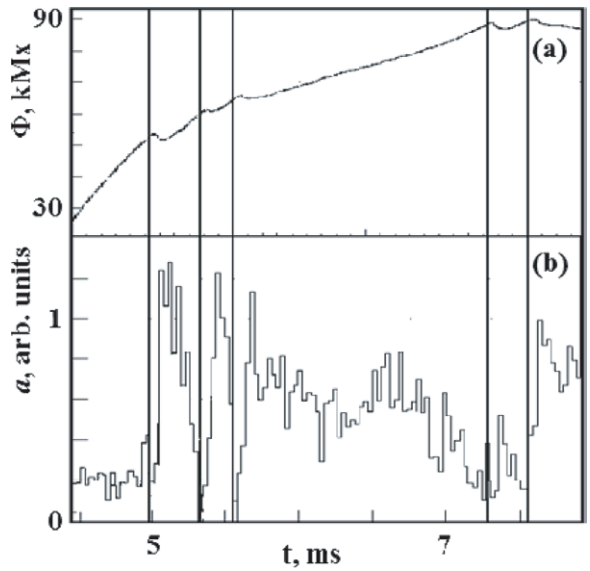

Figure 37. Time evolution of plasma diamagnetism at the turning point (a) and envelope of oscillations with frequency 1.15 MHz (b).

power up to 3 MW were injected into the GDT plasma instead of H^0-beams. From the decay time of accumulated fast ion energy content, it was calculated that the global energy lifetime of fast D^+-ions is ~1.5 time longer than for H^+ ones. The longitudinal profiles of the fusion products (2.45 MeV neutrons and 3.02 MeV protons) emission were measured using an array of scintillation detectors. The detectors were used with and without special collimators. Without the collimator they see $\sim 2\pi$ solid angle.

When collimated by a slit array oriented perpendicularly to the machine axis, the detector essentially measures the DD proton linear specific yield with a spatial resolution of ~20 cm. The experimental results of proton flux measurements are presented in [106]. The scintillation detector data show a higher fusion reaction yield near the turning points than at the mid-plane, in agreement with the codes. Figure 36 also shows how the peak of neutron yield is sensitive to enhancement in ion–ion scattering compared with the classical one represented by the curves calculated using the MCFIT code [101]. As seen from figure 36, the experimental data reasonably agree with the simulation results. The experimental points (circles) lie reasonably close to the curve, which represents the simulation with classical ion–ion scattering, thus indicating that, indeed, no substantial additional scattering occurs. This is considered to be another important argument supporting the main conclusions about the classical character of fast ion relaxation in the GDT experiment with a high-β plasma. For the measured parameters of the warm bulk plasma, its contribution to beta at the center of the device can be estimated as 0.03, and is negligible near the turning points. In contrast, the fast ion density has strong peaks near the turning points because their angular distribution is anisotropic. This can be seen from the measured axial profile of a specific yield of DD fusion reaction (see figure 36), where Q is the flux per cm of the plasma column length that is proportional to fast ion density squared multiplied by the plasma cross section area. Near the center, a reduction in fast ion density and transverse kinetic energy results in about a 40% smaller fast ion contribution to the total β. Accordingly, taking into account the small contribution from the target plasma, one could conclude that total β has a shallow dip $\leqslant 40\%$ at the mid-plane.

Fast ion kinetic stability at high beta. The micro-stability of the central solenoid has not been a problem for GDT, as it was not in the previous experiments with skew injection of neutral beams, like TMX-U [107]. In the recent experiments with deuterium plasma and neutral beams, a distinct mode at 1.15 MHz (close to $0.5 f_{ci}$ at the mid-plane) was detected, as shown in figure 37. Axial wave length was measured to be $\lambda_\parallel = 104 \pm 4$ cm. At present, these fluctuations are relatively weak and do not affect confinement, except that they correlate with some 'saw-teeth' oscillations observed in the measurements of plasma diamagnetism at the fast ion turning points (see figure 22(b)). In GDT, we generally find only a weak heating of the end-loss ions correlated with the onset of fluctuations. For comparison in a regime without fluctuations the mean energy of end-loss ions is measured to be $\langle E \rangle = 1 \pm 0.03$ keV and increases to 1.1 ± 0.03 keV when the fluctuations appear [108].

Because these fluctuations have frequencies less than the minimum ion-cyclotron frequency, this mode may be the AIC mode [109] rather than that of a higher frequency loss-cone instability [110]. The AIC mode is driven by an anisotropic ion energy distribution ($P_\perp / P_\parallel > 1$) as would be generated by NBI. However, in the GDT conditions for instability development are generally more unfavorable considering less anisotropy provided with skew injection of the beams and steep gradients of the plasma parameters. The corresponding modification of the instability threshold and the characteristics of the unstable perturbations are considered in [111]. It

suggests that instability is driven by the newly trapped fast ions at the mid-plane, where their anisotropy is maximal and energy spread is small. The instability is convective and the waves propagate to the ends of the solenoid and dump. These theoretical results were found to be in agreement with experimental observations that suggest that a polarization vector of the oscillations rotates in the direction of ion rotation in the magnetic field and the wave propagates from the center of the solenoid to the ends. Then, the observed 'saw-teeth' relaxations in plasma diamagnetism at the turning points can be explained by axial redistribution of plasma pressure due to an increase in the angular spread of the ions that are in resonance with the unstable wave.

6. Bulk plasma energy and particle losses

Very large electron heat losses to the end wall have been a longstanding past concern about the viability of magnetic-mirror systems. However, the experimental results and theory reviewed in [55] show that there is no fundamental limitation on the electron temperature imposed by the parallel heat losses unless there is strong secondary emission from the end wall. Simple estimates indicate that for the conditions of the GDT experiment, sufficiently strong electron emission from the end wall and substitution of hot electrons by cold secondary ones would, in contradiction with the experimental results, hold electron temperatures below 100 eV and rapidly cool energetic ions by electron drag. The large expansion of the plasma exhaust beyond the end mirrors, as has been predicted by theory [55, 112], decoupled hot electrons confined in the mirror cell from the end walls. As a result, the electron temperature routinely exceeded 200 eV during the shots with 3.5–4 MW of neutral beams and gas puff at the plasma periphery. Higher electron temperatures, approaching 260 eV, were obtained in the regime with a smaller plasma density ($(1–2) \times 10^{19}$ m^{-3}), which was realized by the corresponding reduction in the gas puff [97]. These values are well above the range expected if electron thermal losses to the end walls are dominant. In contrast, the electron temperature (see figure 38) in the GDT experiment is consistent with the modeling, some details of which are given below, which does not suggest this mechanism of energy losses. The longitudinal plasma-energy confinement is of fundamental importance when analyzing the viability of fusion reactors or NSs based on GDT or other open confinement systems. Therefore, the idea of suppressing the electron heat flux by means of a magnetic expander needs direct experimental proof. This section is mainly devoted to such experiments. A review of the theoretical ideas regarding the mechanisms of axial plasma losses is also given. Note that under typical conditions of the GDT experiment and the GDT-based NS the mean free path of electrons leaving the device is much larger than the distance between the mirror and the end wall, i.e. the hot electrons are in a more deeper kinetic regime, at least in the end tank. In the following, we will assume that this approximation is always valid. In the opposite limit, the two-fluid transport equations can be applied for the analysis [113].

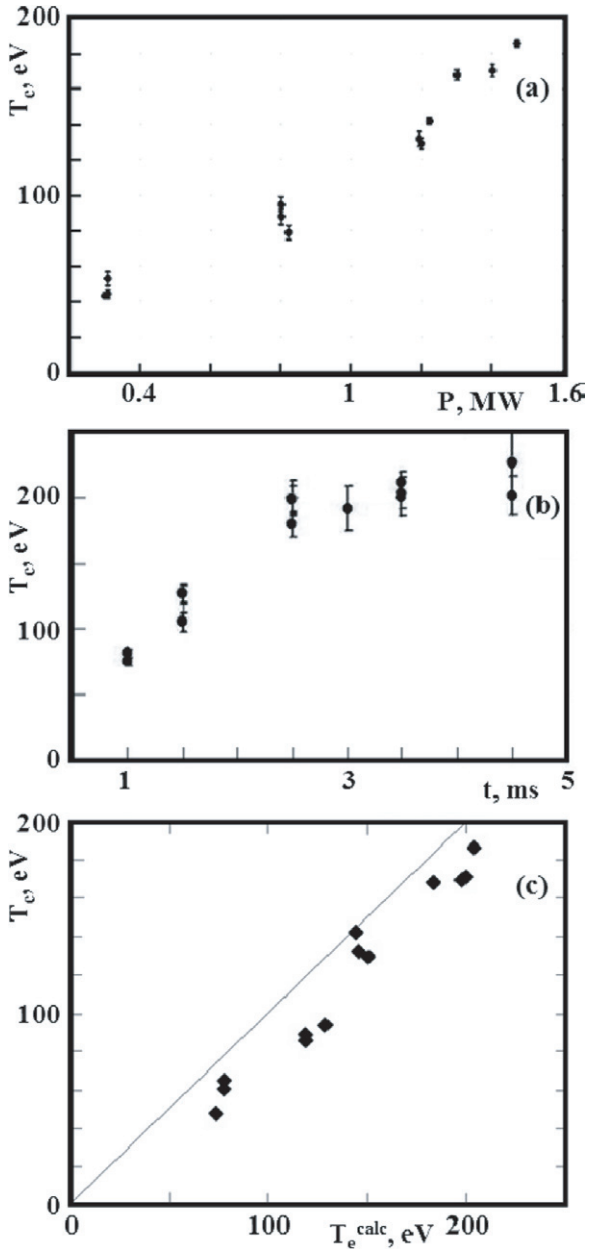

Figure 38. Electron temperature in GDT (*a*) versus trapped power of neutral beams and (*b*) versus time. (*c*) Comparison of the estimated and the experimentally measured electron temperature; the solid line shows $T_e = T_e^{calc}$.

As was mentioned above, the possibility of fast cooling due to direct plasma contact to the end wall is sometimes considered as an inevitable problem related to plasma confinement in magnetic-mirror devices. The mechanism of cooling essentially involves the replacement of the hot electrons leaving the central region of the device along the magnetic-field lines through the magnetic mirror with the secondary cold electrons emitted from the wall. However, in the GDT there is a magnetic nozzle (an expander) designed to allow the plasma flowing out from the device to gradually expand. Let H_m and H_w denote the magnetic fields in the mirror and on the wall, respectively. In the GDT, their ratio H_m/H_w is typically in the range 100–1000. Neglecting the relatively small effect of ion acceleration in the region beyond

the mirror throat, in the rough approximation, one can consider the flow velocity as a constant. Then, from the continuity equation it follows that during the expansion plasma density reduces following to the increasing area of the magnetic flux tubes. Therefore, the plasma density in the expander decreases near the end wall as $n_w/n_{mirror} = H_w/H_m$, and becomes substantially less than that inside the trap. This gives rise to an ambipolar potential in the expander, which forms a potential well for the electrons whose depth increases when the magnetic field at the end wall reduces. Accounting for ion acceleration makes the potential well even deeper.

The theory [2, 55, 112] suggests a strong reduction in the energy loss if the magnetic field to the wall reduces more than $(M/m)^{1/2}$ times (M and m are the ion and electron masses, respectively), i.e. the expansion is high enough. Formally, if the expansion ratio H_m/H_w substantially exceeds $(M/m)^{1/2}$ the hot central cell electrons become essentially trapped in the deep potential well, and the electron loss becomes much less than the ion loss, in contradiction to the charge neutrality of the confined plasma. At smaller expansion ratios, the electron flux is equalized to the ion flux by the potential jump in the Debye sheath near the wall. At very large expansion ratios, the potential variation between the point where H_m/H_w exceeds $(M/m)^{1/2}$ and the end wall becomes small compared with T_e/e and the distribution function of electrons here significantly differs from the Maxwellian with temperature T_e. The electron distribution function in this region is formed by the scattered transiting electrons and the secondary electrons emitted by the wall. If the number of secondary low-energy electrons, which can be characterized by the secondary emission coefficient η, becomes large enough, which happens then $\eta \geqslant 0.5$, the situation drastically deteriorates. In this case, the quasineutrality constraint is not applicable anymore and, in fact, all the hot electrons are replaced by the secondary ones. Moreover, the accumulation of cold secondary electrons would lead to a reduction in the potential drop in the expander, thereby leading to an uninhibited electron heat loss. In [55], a number of methods to reduce the secondary electron flux are considered including the application of a suppressor grid and end plate tilting. Both these methods utilize the flatness of the profile of the electrostatic potential inside the large part of the expander and the corresponding absence of a strong electric field that would pull the secondary electrons to the main plasma. In [112], it is also mentioned that even there may be no need to apply any active suppression methods since the secondary electrons would be subjected to the fast beam–plasma instability, which may lead to their effective angular scattering and reflection back to the end wall. Herein, the role of the non-steady-state effects is also emphasized, which may play a significant role in pulse experiments, such as the GDT experiment, if the particle collision time and the times of neutral ionization and charge exchange in the end tank are comparable to or much longer than the pulse duration. Details of these considerations can be found in [2].

In the case if the secondary electrons are effectively scattered, the influx of cold secondary electrons through the mirror is determined by the drop of the magnetic field in the expander. Of all the secondary electrons only those can penetrate into the device that fall in the loss cone with a pitch angle Θ satisfying the condition $\sin(\Theta) < (H_w/H_m)^{1/2}$. If the electron velocity distribution is isotropic, the fraction of the secondary-electron flux penetrating into the device is about H_w/H_m (the ratio of the loss-cone solid angle to the total solid angle in velocity space) of their primary flux near the wall. Let J_i be the ion flux density on the wall. Assuming as a worst case infinitely large emissivity of the end wall, the flux densities of primary hot electrons J_e and secondary electrons J_e^* can be estimated as $J_e^* \approx J_e \approx J_i \cdot (M/m)^{1/2}$. Then, the influx of secondary electrons penetrating into the device does not exceed the ion flux from the device, $J_e^* \cdot H_w/H_m = J_i \cdot (M/m)^{1/2} \cdot (M/m)^{1/2} H_w/H_m < J_i$, if $H_m/H_w > (M/m)^{1/2}$. Thus, if there are sufficiently strong mechanisms for electron scattering in the expander that make the electron velocity distribution isotropic, the expansion ratio $H_m/H_w = (M/m)^{1/2}$ is sufficient to prevent fast cooling of the plasma in the central cell.

The experimentally measured electron temperature was compared with a value predicted by a quantitative theory describing the longitudinal losses of particles and energy from a GDT developed in [55, 114]. Of most interest is the regime of a collisionless (Knudsen) plasma flow, when the ion mean free path exceeds the characteristic scale of the transient region near the mirrors. Note that the plasma in the central cell is still assumed to be collisional, i.e. inequality (1) holds. Under these conditions, the calculation of particles and energy losses reduces to an integration of the Maxwellian distribution function over the velocity-space domain corresponding to the particles leaving the device. In the case of equal ion and electron temperatures $T_e = T_i = T$, the problem of collisionless ion flow through the GDT mirror was considered in [2, 55, 114]. For this model, the total drop in the ambipolar potential between the center of the device and the end wall is $eU_w = 5T$ and the particle flux through the mirror is $q = q_e = q_i = 1.53 \cdot n_0 \cdot (T/2\pi m_i)^{1/2}$. The energy flux through the mirror is evaluated as $Q = Q_i + Q_e = (1.7 \cdot q_i \cdot T_i + 6.19 \cdot q_e \cdot T_e) = 7.89 \cdot q \cdot T$. Given the trapped neutral beam power we applied this model to evaluate the electron temperature in the GDT experiment. Note that in the calculations we did not take into account spatial profiles of the plasma parameters. The results of calculations are compared with the experimentally measured electron temperature in figure 38(*c*).

Plasma parameters in the GDT expander such as the mean electron energy, the plasma potential, the fluxes of particles and energy through the mirror, and the energy spectrum of the ions leaving the device were measured to evaluate axial energy losses. The results of the measurements are compared with theoretical predictions [114] for the case of a collisionless plasma flow through the mirrors. In experiments, the plasma parameters ($T_e \geqslant 20\,\text{eV}$ and $n_e \sim 10^{19}\,\text{m}^{-3}$) were chosen to provide the regime of collisionless (Knudsen) ion flow through the GDT magnetic mirrors. Such a regime is of most interest, because it is expected to occur at the plasma parameters required for GDT fusion applications.

The plasma parameters beyond the mirror were measured during both the operation of the plasma gun and with the NBI (after the plasma gun was switched off), which corresponded to different plasma temperatures in the central cell.

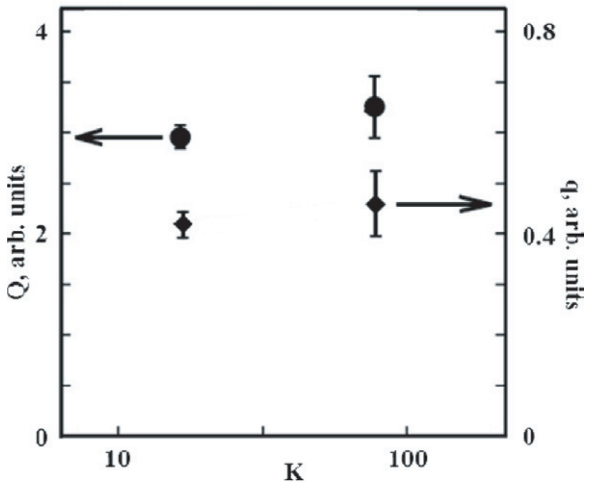

Figure 39. Normalized densities of the energy flux Q and ion flux q in the expander as functions of the expansion ratio.

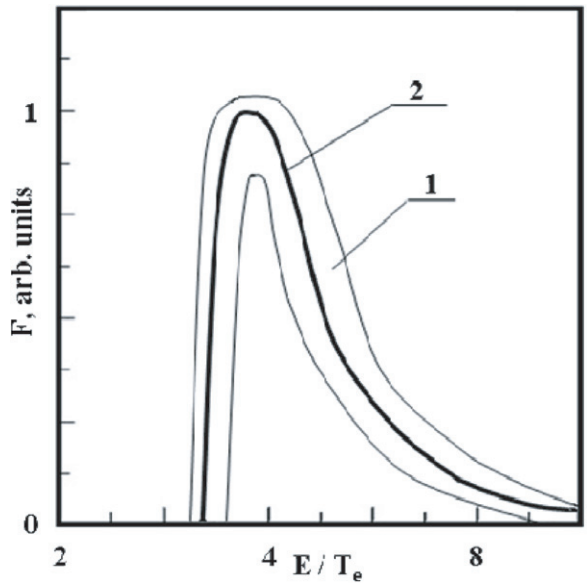

Figure 40. The ion energy distribution function: 1—the region corresponding to the measured distribution functions for different plasma parameters in the central solenoid and 2—a model distribution function.

In experiments aimed at studying the effect of the expander on suppression of the electron heat flux, we used an oxide cathode, 120 mm in diameter, as an emitting wall. The cathode was mounted on a movable support in the expander [115]. The cathode surface was covered with carbonate composition [$BaCO_3$ (50–55%), $SrCO_3$ (40–50%) and $CaCO_3$ (5–8%)] and pressed under a stress of 1000 kgf cm^{-2}. Before the beginning of the experiments, the cathode was baked out for 24 h at a temperature of approximately 500 °C; then the temperature was raised to 950–970 °C in order to decompose the carbonates. In order to monitor the thermo-emission current, an annular molybdenum electrode 2 mm in diameter was mounted around the cathode edge. A 1 kV positive voltage pulse with duration of 20 ms was applied to the electrode. The measured current through the electrode was 7 A; this corresponded to the emission current density $j_T \sim 2$ A cm^{-2}. Consequently, in our experiments, the current density from the surface of the plasma absorber exceeded the current density produced by the electron flow arriving at the plasma dump from the device; thus, the emissivity of the surface of the plasma absorber could be considered to be infinitely large.

Figure 39 shows the normalized ion current density q_i and energy flux Q_{ie} on the expander axis for two values of the expansion ratio $K = H_m/H(z)$ corresponding to two points on the z-axis. The ion current density measured by the movable grid probe is normalized to $n \cdot (T_e)^{1/2}/K$, where T_e and n are the electron temperature and plasma density in the central cell, respectively. In these units, the average value of the normalized ion flux density in the expander is 0.45±0.1. The energy flux density measured by a movable bolometer is normalized to $n \cdot (T_e)^{3/2}/K$.

By dividing the average value of the energy flux density in the expander by the ion flux density, it is possible to obtain the average energy (per one electron–ion pair) carried away from the device. Taking into account the reflection coefficient of the bolometer surface (which is [116] ∼0.2–0.4), we obtain that this energy is $(8.7 \pm 1.8) \cdot T_e$, where T_e is the electron temperature at the center of the device (in energy units).

The ion distribution functions in longitudinal energy, which were measured by the ELA on the end wall on the expander axis, are shown in figure 40. The shaded region presents the experimental data for different values of the electron temperature. For comparison, in the same figure, we show the distribution function calculated by the collisionless-flow model [117]. It is seen that the calculated curve is in good agreement with the measured distributions. From analysis of these data, a conclusion can be drawn that, for a plasma temperature above 20 eV, the ion flow through the mirror is collisionless. This statement is confirmed by an estimate for the mean free path of ions λ_i. For the experimental parameters mentioned above, we have $\lambda_i \approx 120$ cm, which exceeds the characteristic size of the magnetic-mirror region.

It should be noted that the longitudinal energy of ions in the analyzer differs only slightly from their total energy, because the magnetic field near the analyzer is more than 100-fold less than the field in the mirror (from where the ions come out). Therefore, we can assume that the analyzer measures the total ion energy.

By processing the ion energy distribution function, we obtained the value of the mean energy of ions arriving at the plasma absorber to be $(6.5 \pm 0.1) \cdot T_e$. The value of the total drop in the ambipolar potential between the center of the device and the end wall, which was also obtained by processing the ion distribution functions, was $(4.8 \pm 0.1) \cdot T_e$.

The potential profile in the expander beyond the mirror, measured with the use of a local gas target, is presented in figure 41. The closed square presents the value of the potential in the central cell of the GDT, which was obtained by processing the ion distribution function. For comparison, in the same figure, we present the plasma potential profile in the expander calculated from the position of the inflection point in the current–voltage characteristics measured by a movable single probe. Qualitatively, the profile of the potential obtained from probe measurements is similar to that measured with the use of a local gas target: the potential sharply

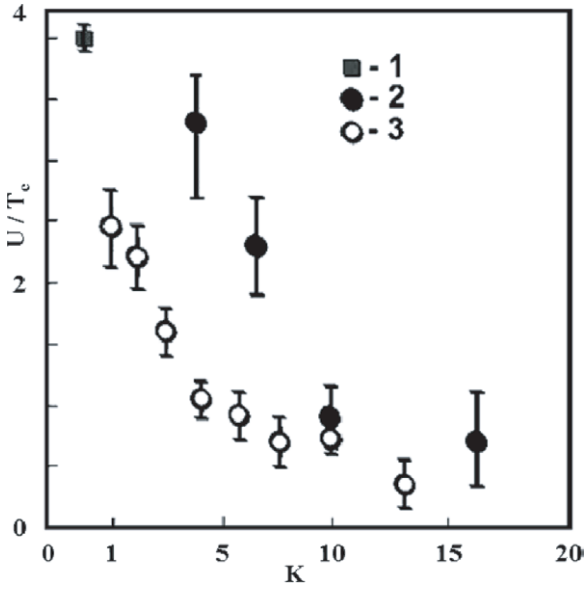

Figure 41. The profile of the electric potential in the expander: 1—energy analyzer data, 2—local gas target data, 3—probe measurements.

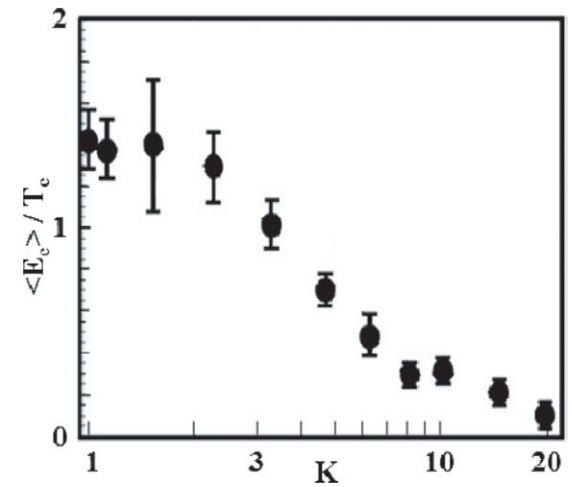

Figure 42. The mean electron energy in the expander as a function of the expansion ratio.

decreases near the mirror and then varies slightly. However, the value of the potential obtained from probe measurements is systematically less by (1–2)·T_e than that measured with the use of a local target (figure 41). Presumably, this is due to plasma perturbations introduced by the probe. These perturbations must be especially large near the mirror, where the transverse size of the plasma is the smallest. The presence of these perturbations was indirectly confirmed by the fact that, with heating (other parameters being the same), the maximum plasma temperature in the device was significantly lower when the probe was introduced in the plasma near the mirror.

The mean electron energy in the expander as a function of the expansion ratio is presented in figure 42. The data are obtained by processing the current–voltage characteristic of a Langmuir probe located in the expander. The mean energy and potential are normalized to the electron temperature in the central cell of the device.

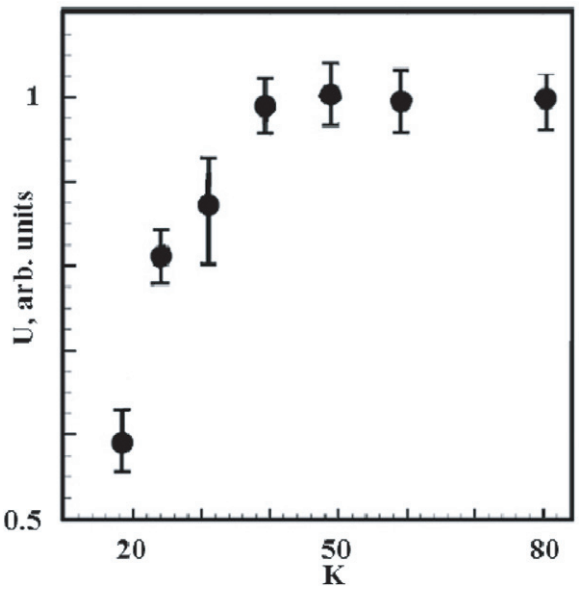

Figure 43. The emissive-probe potential in the central cell of the GDT for different positions of the emissive plasma dump.

The suppression of the electron heat flux from the magnetic-mirror device in the region of an expanding magnetic field beyond the mirrors was confirmed as follows. The heated cathode described above was used as a plasma absorber whose emissivity was assumed to be infinitely large. The magnetic-field expansion ratio at the point at which the plasma receiver was located could be varied in the range 18–20 by moving the receiver along the expander axis (in this case, $H(z)$ was varied) or by changing the magnetic field in the mirror (in this case, H_m was varied). To measure the ambipolar potential in the GDT, we used an emissive probe. Note that an emissive probe cannot be used to measure the plasma potential precisely, because the floating potential of the probe is less than the actual plasma potential by a value close to the electron temperature [118]. In these experiments, the emissive probe was used only to record the sign of the potential and monitor the change in the plasma ambipolar potential on the axis of the device. The projection (along magnetic-field lines) of the emissive plasma absorber on the region where the probe was located was much greater than both the measuring element of the probe and the average error with which the probe was positioned on the axis.

We also studied the dependence of plasma potential in the central solenoid on the magnetic-field expansion ratio in the region where the plasma dump was located. Figure 43 presents the potential of the emissive (flashing) probe in the central cell of the GDT for different positions of the emitting wall. The potential is normalized to the potential of the same probe in the absence of the emitting plasma absorber and is averaged over a series of shots. The positions of the wall along the expander axis are given in units of the expansion ratio K. As is seen in figure 43, for large expansion ratios (>50), the probe potential in the central cell is almost non-sensitive to the position of the emitting wall and its emissivity. As the expansion ratio decreases (K < 40–50), the ambipolar potential drop decreases. This is confirmed by a substantial decrease in the floating potential of the emissive probe and,

consequently, in the plasma potential in the central cell of the GDT. As the ambipolar potential drop between the device and the plasma absorber decreases, the axial energy loss from the device increases because of the increase in the electron heat flux.

The longitudinal thermal flux and profile of the electrostatic potential in the case of a wall, which emits electrons, were considered in [118]. It was shown that, if the secondary-emission coefficient Γ exceeds a certain critical value, the emitted flux is limited to the value Γ_{crit} by the intrinsic space charge. For a hydrogen plasma this theory predicts a critical secondary-emission coefficient of $\Gamma_{crit} = 0.81$, a potential drop of $eU_w = 1.02 \cdot T_e$, and an energy flux of $Q = 0.5 n v_e T_e F(\Gamma)$, where $V_e = (8T_e/\pi m_e)^{1/2}$ and $F(\Gamma)$ is a function that describes the flux limitation by the space charge of secondary electrons. According to [118], for $\Gamma \geqslant \Gamma_{crit}$, $F(\Gamma_{crit}) = 0.38$ and the anomalous heat flux from the device must exceed the directly measured heat flux by a factor of 5. As is seen, the potential drop U_w becomes very small, which was observed in experiments with a thermal cathode near the magnetic mirror in the case of a small expansion ratio (figure 43). In the case of a large expansion ratio (>50), the potential drop is almost independent of the position of the emitting wall and is equal to the potential drop obtained in experiments with an ordinary stainless-steel plasma absorber at room temperature. This is considered as evidence of the suppression of the electron heat flux to the end wall.

As was noted at the beginning of this section, the mechanism for this suppression can be associated with both the tendency of the electron distribution function to become isotropic due to intense scattering by electromagnetic-field microfluctuations in the case of a developed turbulence and the accumulation of trapped electrons in the well of the effective Yushmanov's potential in the expander [112, 114]. The population of cold trapped electrons can be produced, e.g., in the course of the filling of the device with a plasma before the beginning of NBI heating, when the electron temperature is still low (~5 eV) and the plasma flow is collisional. Another reason for the production of cold trapped electrons is a weak electron scattering in the collisionless plasma flow in the expander. The space charge of the accumulated electrons can prevent the penetration of the secondary electrons into the central cell and, thus, suppress the anomalous electron heat flux [118]. The presence of cold trapped electrons in the expander is confirmed by the measured potential profiles and the value of the mean electron energy (figures 41 and 42). According to the discussed collisionless-flow model [114], if there are no trapped cold electrons in the expander, the mean electron energy should not change along the magnetic-field line. In our experiments (in contrast to the OGRA-4 experiments [119]), because of good vacuum conditions, cooling of electrons beyond the mirrors due to additional ionization of a residual gas in the expander is low. Without electron scattering, the electric potential should be almost constant along the expander, and only drops in a narrow Debye layer. However, the experiments show a monotonic decrease in the mean electron energy and potential along the expander. This clearly indicates that cold electrons trapped in the expander between the mirror and the wall play an important role in the formation of the potential profile in the expander.

The results obtained in these experiments can be summarized as follows.

- The energy flux onto the plasma absorber in the expander is mainly determined by the ions; the electron heat flux is relatively small.
- The experimentally measured ion energy distribution functions in the expander agree well with the calculations based on the model of a collisionless plasma flow.
- The energy carried away by a single ion–electron pair is, on average, larger than the plasma temperature in the central cell by a factor of 8.7 ± 1.8; the average energy carried away by an ion is $(6.5 \pm 0.1) \cdot T_e$; and the measured total potential drop of the ambipolar potential is $(4.8 \pm 0.1) \cdot T_e$. These values agree well with the calculations based on the model of a collisionless plasma flow.
- The measured profiles of the electrostatic potential and the mean electron energy indicate the presence of trapped electrons in the expander.
- It is shown that, if the ratio between the magnetic field in the mirror and that at the wall of the plasma absorber is higher than 40–50, the suppression of the electron heat flux from the device occurs independently of the emissive properties of the wall.

7. Conclusions

On the basis of the experimental results presented in this paper the following conclusions can be drawn:

(1) Plasma in the axisymmetric solenoid of the GDT device is successfully stabilized against excitation of MHD instability by the application of external MHD anchors, in which the plasma is fed by particle exhaust through the mirrors. In particular, an expander or cusp end cells were used to stabilize the plasma. Confinement with suppressed transverse losses is also demonstrated in the regime with an unfavorable pressure-weighted curvature when a sheared plasma rotation (vortex) is produced at the periphery by biasing of radial limiters and segments of the end plate.

(2) In the GDT, electron heat losses are inhibited by strong flaring of the magnetic field in the end tank. A drop in plasma density in the decreasing magnetic field beyond the mirrors results in the formation of a deep electrostatic potential well for electrons in the central solenoid, which prevents the majority of them from reaching the end plate. This also flattens the potential profile in the outer part of the end tank. Under these conditions, the secondary cold electrons emitted by the end wall cannot penetrate into the central solenoid and drain the energy from it. Therefore, the axial heat losses from the GDT are not dominated by the electron heat losses, but rather by the plasma exhaust through the end mirrors. It was found that the axial particle and energy losses are consistent with the model of gas-dynamic flow of the collisional plasma through the mirrors. The axial losses through the

end mirrors dominate in the energy balance of the plasma heated by neutral beam injection. The transverse losses do not exceed 15%.

(3) The relaxation of fast ions produced in the GDT by injection of skew neutral beams near the mid-plane of the central solenoid is governed by classical mechanisms of slowing down of plasma electrons and ion–ion scattering. Only at the highest plasma betas was excitation of AIC instability detected, which however did not induce either enhanced fast ion losses or axial broadening of fast ion density peaks near their turning points.

The successful operation with $\beta \leqslant 60\%$, classical ions and electrons with T_e up to 260 eV of the GDT device extrapolates to a 2 MW m^{-2} D–T neutron source, which burns only ~0.1 kg of tritium per full power year. The GDT-based neutron source has no serious physics, engineering or technology constraints. It provides a neutron spectrum similar to that of ITER and DEMO and satisfies the missions specified by the materials community to test fusion materials.

In addition to the application of the GDT as a neutron source, the collisional GDT solenoid with high-field mirror coils is well suited for plasma–wall interaction studies. The plasma exhaust through the ends can be controlled by varying the beam injection power and gas fueling rate over a wide range of interests for tokamak divertor studies. When the plasma is terminated at the mirror throats by a material wall, the power flux through electron heat conduction in this region would be in the range of several 100 MW m^{-2}. In this case, the electron and ion energies would be 100–200 eV. Studies with hydrogen, deuterium and tritium can be carried out. This possibility has been demonstrated by the measurements of power density onto a tungsten target placed in the GDT plasma near the end mirror which exceeds 160 MW m^{-2} with an electron temperature in the central cell of 140 eV.

The plasma electron temperature in the GDT experiment is determined by a balance of energy transfer from fast injected ions and plasma exhaust through the mirrors. In high-performance shots when the temperature exceeds 150 eV, the electron temperature and plasma density pulses did not reach a steady state within 5 ms. Further extension of the pulse duration (to at least 20 ms for $T_e = 200$ eV) is still required to reach steady-state conditions in the experiments. Therefore, the electron temperature in the GDT can be increased by the extension of the NB pulse, which should be accompanied by an increase in the magnetic field to keep the plasma below the ballooning instability threshold. This is planned to realize in subsequent upgrades of the GDT device. Application of ECR heating near the end mirrors is also planned to increase the electron temperature in the GDT [120].

Longer term plans in development of mirror devices in the Budker Institute are connected with the concept of a gas-dynamic multiple-mirror trap (GDMT) [121]. The GDMT is proposed to combine the GDT properties with good plugging capability of multi-mirror traps. The primary aim of the project is to prove the concept of a steady-state multiple-mirror fusion reactor, and obtain confinement scaling, while going to longer pulses and higher electron temperatures than those available in a GDT. The secondary mission of GDMT is to be a prototype of an energy-effective neutron source to replace the unrealized project of the 'Hydrogen Prototype' [122].

Acknowledgments

The authors acknowledge support from D D Ryutov who initiated the appearance of this paper and whose pioneering works together with V V Mirnov and other colleagues formed the concept of the gas-dynamic trap and the GDT-based neutron source. They also would like to thank their colleagues from the Budker Institute who made significant contributions to the scientific results, including A V Anikeev, P A Bagryansky, A D Beklemishev, I A Kotelnikov, A A Lizunov, K V Lotov, V V Maximov, S V Murakhtin, E I Soldatkina, Yu A Tsidulko and others. Contributions from K Noack (FZR, Germany), V Robouch (ENEA, Frascati, Italy), U Fisher and A Moeslang (KF Karlsruhe, Germany), D J Den Hartog (UW, USA) are also highly appreciated. The authors are grateful to T C Simonen for valuable discussions and encouragement. They also thank M V Ivantsivsky and V H Amirov for their assistance with preparation of the figures. Assistance of B Ferguson and A Smirnov, who read the manuscript and made valuable suggestions, is highly appreciated.

This work was financially supported by the Ministry of Education and Science of the Russian Federation, by the Russian Government project 11.G34.31.0033, the Presidium of the Russian Academy of Sciences program No 30, the Council of the Russian Presidential Grants project NSh-5118.2012.2, RFBR (grants No 12-02-31632, No 12-07-31185).

References

[1] Mirnov V V and Ryutov D D 1979 *Sov. Tech. Phys. Lett.* **5** 279
[2] Mirnov V V and Ryutov D D 1988 Gas-dynamic trap *Itogi Nauki i Tekhniki—Fizika Plazmy*, (Moscow: The Publishing House of the Institute of Scientific Information) vol 8 p 77
[3] Kotel'nikov I A, Mirnov V V, Nagornyj V P and Ryutov D D 1985 *Plasma Physics and Controlled Nuclear Fusion Research* 1984 (Vienna: IAEA) vol II p 309
[4] Ryutov D D 1990 *Plasma Phys. Control. Fusion* **32** 999
[5] Ivanov A A and Ryutov D D 1990 *Nucl. Sci. Eng.* **106** 235
[6] Anikeev A V *et al* 1996 *Proc. 23th EPS Conf. on Plasma Physics and Controlled Fusion (Kiev, Ukraine)* vol 20C, part 2 pp 688–91
[7] Coensgen F H *et al* 1989 *J. Fusion Energy* **8** 237
[8] Hershkowitz N 1990 Mirror devices *Nucl. Fusion* **30** 1761
[9] Yasaka Y *et al* 1989 *Plasma Physics and Controlled Nuclear Fusion Research* 1988 vol 2 p 727
[10] Ferron J R *et al* 1983 *Phys. Rev. Lett.* **51** 1955
[11] Post R F 2010 *Fusion Sci. Technol.* **57** 335
[12] Ryutov D D 1988 *Sov. Phys.—Usp.* **31** 300
[13] Kesner J, Horne S F and Pastukhov V P 1987 *J. Fusion Energy* **4** 401
[14] Casey *et al* 1988 *Phys. Fluids* **31** 2009
[15] Li X Z, Kesner J and Lane B 1985 *Nucl. Fusion* **25** 907
[16] Ryutov D D and Stupakov G V 1985 *JETP Lett.* **26** 174
[17] Ryutov D D and Cohen R H 2004 *Contrib. Plasma Phys.* **44** 168
[18] Phaedrus group 1985 *Nucl. Fusion* **25** 1213
[19] Akhmetov T D *et al* 2005 *Trans. Fusion Sci. Technol.* **47** 23

[20] Ryutov D D and Stupakov G V 1981 *8th Int. Conf. on Plasma Physics and Controlled Nuclear Fusion Research (Brussels, Belgium, 1980)* (Vienna: IAEA) vol 1, p 119
[21] Kaiser T B and Pearlstein L D 1983 *Phys. Fluids* **26** 3053
[22] Post R F 1987 *Nucl. Fusion* **27** 1579
[23] Dimov G I, Zakaidakov V V and Kishinevsky M E 1977 *Proc. 6th Int. Conf. on Plasma Physics and Controlled Nuclear Fusion Research (Berchtesgaden, West Germany, 1976)* (Vienna: IAEA) paper no C4 *Sov. J. Plasma Phys.* **2** 826
[24] Fowler T K and Logan B G 1977 *Comment. Plasma Phys. Control. Fusion* **2** 167
[25] Baldwin D E and Logan B G 1979 *Phys. Rev. Lett* **43** 1318
[26] Anikeev A V, Bagryansky P A, Deichuli P P, Ivanov A A, Karpushov A N, Maximov V V, Podminogin A A, Stupishin N V and Tsidulko Y A 1997 *Phys. Plasmas* **4** 347
[27] Lane B, Post R S and Kesner J 1987 *Nucl. Fusion* **27** 277
[28] Post R F 2001 *Fusion Sci. Technol.* **39** 25
[29] Post R F 2003 *Fusion Sci. Technol.* **43** 195
[30] Post R F, Fowler T K, Bulmer R, Byers J, Hua D and Tung L 2005 *Fusion Sci. Technol.* **47** 49
[31] Beklemishev A D 2011 *Fusion Sci. Technol.* **59** 90
[32] Bagryansky P A *et al* 1999 *Trans. Fusion Technol.* **35** 79–86
[33] Stacey W M 2011 *Proc. Int. Conf. on Fusion for Neutrons and Subcritical Nuclear Fission (Varenna, Italy, 12–15 September)* p 31
[34] Moir R W, Martovetsky N N, Molvik A W, Ryutov D D and Simonen T C 2012 *Fusion Sci. Technol.* **61** 206
[35] Bagryansky P A *et al* 2004 *Fusion Eng. Des.* **70** 13
[36] Sorokin A *et al* 2010 *Rev. Sci. Instrum.* **81** 02B108
[37] Robouch B V *et al 1995 Proc. IEEE—SOFE (Urbana, IL)* vol 2 pp 1131–4
[38] Fischer U, Moeslang A and Ivanov A A 1999 *Trans. Fusion Technol.* **35** 160
[39] Fischer U and Dalle Donne M 1997 *4th Int. Symp. on Fusion Nuclear Technology (Tokyo, Japan, 6–11 April)*
[40] Ehrlich K and Daum E (ed) 1994 *Proc. IAEA Workshop on Intense Neutron Sources (Karlsruhe, Germany, 21–23 September 1992)* KfK Report 5296
[41] The IFMIF CDA Team 1977 International Fusion Materials Irradiation Facility. Conceptual Design Activity, ed M Martone *ENEA Frascati Report* RT/ERG/96/11 (December 1976) 1977 *Nucl. Instrum. Methods* **145** 1 (Special issue devoted to different projects of plasma based neutron sources)
[42] Jung P, Hishinuma A, Lucas G E and Ullmaier H 1996 *J. Nucl. Mater.* **232** 186
[43] Ryutov D D, Baldwin D E, Hooper E B and Thomassen K I 1998 *J. Fusion Energy* **17** 253
[44] Moir R W and Rognlien T D 2007 *Fusion Sci. Technol.* **52** 408
[45] Noack K *et al* 2008 *Ann. Nucl. Energy* **35** 1216–22
[46] Kruglyakov E P 2001 *Trans. Fusion Sci. Technol.* **39** 57
[47] Deichuli P P 2012 private communication
[48] Moir R W, Martovetsky N N, Molvik A W, Ryutov D D and Simonen T C 2012 *Int. Conf. on Fusion for Neutrons and Subcritical Nuclear Fission (Varenna, Italy, 12–15 September 2011) AIP Conf. Proc.* **1442** 43
[49] Ryutov D D 2012 *Int. Conf. on Fusion for Neutrons and Subcritical Nuclear Fission (Varenna, Italy, 12–15 September 2011) AIP Conf. Proc.* **1442** 247
[50] Lotov K V and Ivanov A A 2000 *Plasma Phys. Control. Fusion* **42** 1077
[51] Ivanov A A *et al* 1994 *Phys. Plasmas* **1** 1529
[52] Coensgen F H *et al* 1990 *Nucl. Sci. Eng.* **106** 138
[53] Post R F and Ryutov D D 1995 *Comment. Plasma Phys. Control. Fusion* **16** 375
[54] Baldwin D E 1977 *Rev. Mod. Phys.* **49** 317
[55] Ryutov D D 2005 *Fusion Sci. Technol.* **47** 148
[56] Anikeev A V, Bagryansky P A, Kuznetsov G I and Stupishin N V 1999 *Plasma Phys. Rep.* **25** 775
[57] Deichuli P P, Davydenko V I, Ivanov A A, Korepanov S A, Mishagin V V, Sorokin A V, Stupishin N V and Shulzhenko G I 2004 *Rev. Sci. Instrum.* **75** 1816
[58] Bagryansky P A *et al* 1999 *J. Nucl. Mater.* **265** 124
[59] Bagryansky P A *et al* 1994 *Plasma Phys. Rep.* **20** 176
[60] Berezovskii E L, Kislyakov A I, Petrov S Ya and Roslyakov G V 1980 *Sov. J. Plasma Phys.* **6** 760
[61] Tammen H F, Donne A J, Oyevaar T and Shuller F C 1993 *Plasma Phys. Rep.* **20** 158
[62] Abdrashitov G F *et al* 2000 *Rev. Sci. Instrum.* **72** 594
[63] Anikeev A V *et al* 1998 *ICPP and 25 EPS CCFPP (Prague)* ed P Pavlo vol 22C (ECA) pp 1498–501
[64] Bagryansky P A, Deichuli P P, Ivanov A A, Korepanov S A, Lizunov A A, Murakhtin S V, Savkin V Ya, Den Hartog D J and Fiksel G 2003 *Rev. Sci. Instrum.* **74** 1592
Lizunov A A, Den Hartog D J, Donin A S, Ivanov A A, Prikhodko V V 2011 *Rev. Sci. Instrum.* **82** 086105
[65] Davydenko V I and Ivanov A A 2004 *Rev. Sci. Instrum.* **75** 1809
[66] Anikeev A V *et al* 1994 *Fiz. Plazmy* **20** 192 (in Russian)
[67] Korepanov S A, Bagryansky P A, Deichuli P P, Ivanov A A and Tsidulko Yu A 1999 *Trans. Fusion Technol.* **35** 345
[68] Zinoviev A N, Krizhanovski E R, Ivanov A A and Klesov V V 1990 Budker Institute of Nuclear Physics, Novosibirsk (in Russian) Preprint 90-20
[69] Medley S S, Donné A J H, Kaita R, Kislyakov A I, Petrov M P and Roquemore A L 2008 *Rev. Sci. Instrum.* **79** 011101
[70] Davydenko V I *et al* 1997 *Plasma Phys. Rep.* **23** 427
[71] Prikhodko V V and Murakhtin S V 2005 *Trans. Fusion Sci. Technol.* **47** 315
[72] Molvik A W *et al* 1990 *Nucl. Fusion* **30** 815
[73] Ivanov A A 1993 *Bull. Am. Phys. Soc.* **38** 2072
[74] Rosenbluth M N and Longmire C L 1957 *Ann. Phys.* **1** 20
[75] Ryutov D D 1987 *Proc. Workshop Int. School of Plasma Physics (Varenna, 1–11 September)* pp 791
[76] Anikeev A V, Bagryansky P A, Ivanov A A and Kotelnikov I A 1995 *Plasma Phys. Control. Fusion* **37** 1239
[77] Berk H L, Ryutov D D, Stupakov G V and Tsidulko Yu A 1991 *Plasma Physics and Controlled Nuclear Fusion Research* 1990 (Vienna: IAEA) vol II p 289
[78] Tsidulko Yu A 1992 Budker Institute of Nuclear Physics, Novosibirsk, Preprint 92-10
[79] Bagryansky P A, Ivanov A A, Klesov V V, Kotel'nikov I A, Karpushov Yu I, Roslyakov G V, Tsidulko Yu A, Bruen R A, Molvik A W and Casper T A 1991 Experimental MHD stability limit in the gas-dynamic trap *Plasma Physics and Controlled Nuclear Fusion Research* 1990 (Vienna: IAEA 1991) vol 2 p 655
[80] Bagryansky P A 2000 *Doctor Thesis* Novosibirsk
[81] Molvik A W, Casper T A and Futch A H 1990 *Nucl. Fusion* **30** 1061
[82] Molvik A W, Breun R A, Golovato S N, Hershkowitz N, McVey B, Smatlak D and Yujiri L 1982 *Phys. Rev. Lett.* **48** 742
[83] Berk H L, Rosenbluth M N, Wong H V, Antonsen T M Jr and Baldwin D E 1983 *Sov. J. Plasma Phys.* **9** 108
[84] Anikeev A V *et al* 1992 *Plasma Phys. Control. Fusion* **34** 1185
[85] Rosenbluth M N, Krall N A and Rostoker N 1962 *Nucl. Fusion* (Suppl) **2** 143 part 1
[86] Sato T *et al* 1987 *Plasma Physics and Controlled Nuclear Fusion Research Proc. 11th Int. Conf. (Kyoto, Japan, 1986)* (Vienna: International Atomic Energy Agency) vol 2 p 343

[87] Dimov G I, Davidenko V I and Lysyansky P B 1989 *Proc. 16th European Conf. on Controlled Fusion and Plasma Physics (Venice)* ed S Segre *et al* (Petit-Lancy: European Physical Society) vol 2 p 815

[88] Adati K *et al* 1981 *Plasma Physics and Controlled Nuclear Fusion Research 1986 Proc. 8th Int. Conf. (Brussels, Belgium, 1981)* (Vienna: IAEA) vol 1 p 143

[89] Sakai O, Yasaka Y and Itatani R 1993 *Phys. Rev. Lett.* **70** 4071

[90] Sakai O, Yasaka Y and Itatani R 1993 *Proc. Int. Conf. on Open Plasma Confinement Systems for Fusion (Novosibirsk)* ed A Kabantsev p 197 (Singapore: World Scientific)

[91] Bekhtenev A A and Volosov V I 1977 *Sov. Phys. Tech. Phys.* **22** 834

[92] Ellis R 2008 *Bull. Am. Physical Soc.* **53** 75 (papers CP6 92 to 97)

[93] Cho T *et al* 2007 *Fusion Sci. Technol.* **51** 11

[94] Bekhtenev A A, Volosov V I, Ellis R A and Yudin Yu N 1970 Budker Institute of Nuclear Physics, Novosibirsk, Preprint 37-70

[95] Sorokina E A 2009 *Plasma Phys. Rep.* **35** 426

[96] Beklemishev A D, Bagryansky P A, Chaschin M S and Soldatkina E I 2010 *Fusion Sci. Technol.* **57** 351

[97] Ivanov A A *et al* 2010 *Fusion Sci. Technol.* **57** 322

[98] Ivanov A A *et al* 2003 *Phys. Rev. Lett.* **90** 105002

[99] Prikhodko V V, Bagryansky P A, Beklemishev A D, Kolesnikov E Yu, Kotelnikov I A, Maximov V V, Pushkareva A N, Soldatkina E I, Tsidulko Yu A and Zaytsev K V 2011 *Trans. Fusion Sci. Technol.* **59** 94

[100] Kesner J 1973 *Plasma Phys.* **15** 577
Kesner J 1980 *Nucl. Fusion* **20** 557

[101] Noack K, Otto G and Collatz S 1999 *Trans. Fusion Technol.* **35** 218

[102] Collatz S and Noack K 1999 *Trans. Fusion Technol.* **35** 375

[103] Anikeev A V *et al* 2000 *Nucl. Fusion* **40** 753

[104] Kornilov V N and Maximov V V 2001 *Instrum. Exp. Tech.* **44** 219

[105] Prikhodko V V, Anikeev A V, Bagryansky P A, Lizunov A A, Maximov V V, Murakhtin S V and Tsidulko Yu A 2005 *Plasma Phys. Rep.* **31** 899

[106] Maximov V V, Anikeev A V, Bagryansky P A, Ivanov A A, Lizunov A A, Murakhtin S V, Noack K and Prikhodko V V 2004 *Nucl. Fusion* **44** 542

[107] Simonen T C *et al* 1983 *Phys. Rev. Lett.* **50** 1668

[108] Bagryansky P A *et al* 2011 *Book of abstracts of the 38th Int. (Zvenigorod) Conf. on Plasma Physics and Controlled Fusion (Zvenigorod, Moscow, 14–18 February)* p 35 (in Russian)

[109] Davidson R C and Ogden J M 1975 *Phys. Fluids* **18** 1045

[110] Post R F and Rosenbluth M N 1966 *Phys. Fluids* **9** 730

[111] Chernoshtanov I S and Tsidulko Yu A 2011 *Fusion Sci. Technol.* **59** 116

[112] Konkashbaev I K, Landman I S and Ulinich F R 1978 *Sov. Phys.—JETP* **47** 501

[113] Braginski S I 1965 Transport processes in plasma *Reviews of Plasma Physics* vol 1, ed M A Leontovich (New York: Consultants Bureau) p 205

[114] Mirnov V V and Tkachenko O A 1986 Budker Institute of Nuclear Physics, Novosibirsk, Preprint 86-26

[115] Kuznetsov G I 1997 *Proc. 3rd Workshop Pulsed RF Source for Linear Collider (RF96) (April) KEK Conf.* 97-1 ed S Fuguta, part A, p 262

[116] Kurnaev V A, Pashkova E S and Molchanov V A 1985 *Otrazhenie legkikh ionov ot poverkhnosti tverdogo tela* (*Reflection of Light Ions from Solid Surfaces*) (Moscow: Energoatomizdat)

[117] Mirnov V V and Ryutov D D 1980 *Vopr. At. Nauk. Tekh. Termoyademyj Sintez* **1** 57

[118] Hobbs G D and Wesson J A 1967 *Plasma Phys.* **9** 85

[119] Bogdanov G F, Golovin I N, Kucheryaev Y A and Panov D A 1962 *Nucl. Fusion* (Suppl.) **2** 215 part 1

[120] Bagryansky P A *et al* 2012 *Proc. 9th Int. Conf. on Open Magnetic Systems for Plasma Confinement (Tsukuba, 27–31 August) Fusion Engineering and Design* submitted

[121] Beklemishev A *et al* 2012 Fusion for neutrons and subcritical nuclear fission *AIP Conf. Proc.* **1442** 147

[122] Anikeev A V *et al* 2006 *33th European Physical Society Conference on Controlled Fusion and Plasma Physics (Rome, Italy, 19–23 June)* vol 30I (ECA) p 4.078